

Designing Quaternary Hydrides with Potential High T_c Superconductivity

Adam Denchfield,¹ Hyowon Park,^{1,2} and Russell J. Hemley^{1,3,4}

¹*Department of Physics, University of Illinois Chicago, Chicago, Illinois 60607, USA*

²*Materials Science Division, Argonne National Laboratory, Lemont, Illinois 60439, USA*

³*Department of Chemistry, University of Illinois Chicago, Chicago, Illinois 60607, USA*

⁴*Department of Earth and Environmental Sciences,
University of Illinois Chicago, Chicago, Illinois 60607, USA*

(Dated: March 4th, 2024)

We propose three parent structures for designing quaternary hydrides of increasing complexity to optimize parameters correlated with high T_c superconductivity. The first is a simple $\text{Pm}\bar{3}\text{m}$ cell inspired by the FCC RH_3 structures (R = trivalent rare earths), which we show has moderately promising potential for high T_c compounds. The second is an $\text{Fm}\bar{3}\text{m}$ heterostructure inspired by our work on $\text{Lu}_8\text{H}_{23}\text{N}$ that consistently produces metallic hydrogen sublattices, whose quantum interference with Lewis bases is designed to high $\text{DOS}_H(E_F)$. Several examples are put forward that first-principles calculations confirm have hydrogen-dominant metal character, as well as strong network connectivity as measured with the Electron Localization Function (ELF). The third quaternary model structure allows for a more precise description of doping as well as symmetry breaking of octahedral hydrogen which improves the hydrogen network connectivity. These model structures/formulae predict compounds with high predicted T_c and have enough flexibility to optimize for both T_c and stability at low pressures.

I. INTRODUCTION

The synthesis of materials that superconduct at room temperature and atmospheric pressure has been a long-standing dream since the discovery of superconductivity [1]. The theoretical predictions of high T_c superconductivity in metallic hydrogen [2, 3] and its subsequent prediction in dense hydrides [3] have been realized experimentally [4–8] (see [9] for a review), alongside theoretical work studying the chemical precompression effects of hydrogen combined with other elements. Notable in this regard are LaH_{10} [10, 11] which were found to agree closely with experiment [4, 5], followed by later experiments on the YH_n system [6–8] and ternary hydrides [12–14]. Several works have proposed ternary or more complex hydrides as vehicles to lower the pressure needed for high-temperature superconductivity [15–21]. Many such studies start with the highest T_c materials and attempt to alloy them to lower the pressure necessary to stabilize their structures.

In contrast, the approach we consider here is to begin with hydrogen-rich structures that are already stable at ambient conditions (as suggested by Ashcroft [22]) and attempt to dope them optimally for high T_c . Of note are the FCC rare-earth trihydride (RH_3) compounds, which have strong electron-phonon coupling (EPC) [23–26] associated primarily with octahedrally coordinated hydrogen, as in palladium hydrides [27]. Interestingly, the FCC phases can be metastabilized with doping [28], ball milling [29], and quenching [30]. This echoes the Allen and Dynes prediction that structures with very strong electron-phonon coupling can be metastabilized with disorder [31] to allow for arbitrarily large superconducting T_c . In FCC RH_3 , doping the rare earth [32] and substituting nitrogen for octahedral hydrogen in LuH_3 [33, 34] have both been predicted to increase

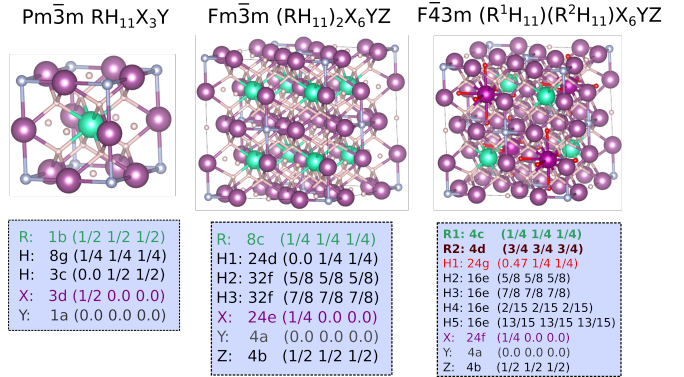


FIG. 1: Three structures of increasing complexity that serve as model structures for quaternary (or even more complex) hydrides.

this electron-phonon coupling. Notably, evidence of superconductivity in near-ambient conditions has been reported for FCC $\text{LuH}_{3-x}\text{N}_y$ [35, 36].

Inspired by our earlier work describing novel $\text{Lu}_8\text{H}_{23}\text{N}$ [37] structures with flat hydrogen-based bands at E_F , we generalize the idea of doping the metal atom in RH_3 to include small amounts of doping of the octahedral hydrogen with Lewis bases [O,N,S,P]. As the space of possible quaternary structures and stoichiometries is huge, we use FCC RH_3 and the results of our previous work [37] to design model structures with relatively few degrees of freedom. We propose three model structures of increasing complexity that are engineered to have dominant hydrogen states at the E_F that emulate metallic hydrogen [22]. These structures are summarized in Fig. 1.

II. METHODOLOGY

We use density functional theory (DFT) [38–40] and DFT+U [41, 42] first-principles electronic structure calculations (see Sec. SI-B) to study the examples built using our proposed model structures (Fig. 1). To study large amounts of stoichiometries in our model structures and try to maximize T_c , we take advantage of the established correlation between certain hydride electronic properties and the isotropic Eliashberg T_c [43], which yields a method to roughly estimate T_c . The T_c estimator takes the form

$$T_c^{net} \approx 750\Phi - 85 \quad (\text{Kelvin}) \quad (1)$$

$$\Phi \equiv \phi_{iso}^{net} \times H_f \times \sqrt[3]{\text{DOS}_{H,rel}(E_F)} \quad (2)$$

$$H_f \equiv \frac{\# \text{ of H forming network}}{\# \text{ of atoms in unit cell}} \quad (3)$$

$$\text{DOS}_{H,rel}(E_F) \equiv \frac{\text{DOS}_H(E_F)}{\text{DOS}_{tot}(E_F)} \quad (4)$$

where ϕ_{iso}^{net} is the critical hydrogen networking isovalue [43] which roughly measures the bonding strength/connectivity of the hydrogen sublattice. It is determined by the isovalue in which the electron localization function (ELF) of electrons centered on different hydrogen atoms begin to overlap. H_f is the fraction of hydrogen in the unit cell forming a network with overlapping ELF from different hydrogen, and $\text{DOS}_{H,rel}(E_F)$ is the relative contribution of hydrogen states to the density of states at E_F . It has been established to reproduce the computed isotropic Eliashberg T_c of hundreds of hydrides within ± 60 K [43].

III. RESULTS AND DISCUSSION

A. $\text{Pm}\bar{3}\text{m RH}_{11}\text{X}_3\text{Y}$ Structure

We present first a simple model structure for quaternary hydrides, with the chemical formula $\text{RH}_{11}\text{X}_3\text{Y}$ (Fig. 2). It is distinguished by a central RH_{11} unit with a typical ELF and PDOS illustrated using LuH_{11} as an example in Fig. 2(c,d) surrounded by an X_3Y 'cage'. In the $\text{RH}_{11}\text{X}_3\text{Y}$ model structure, the hydrogens are placed in the positions they occupy in FCC RH_3 , except for the 1a Wyckoff position which may be occupied by hydrogen or a Lewis base (N,P,O,S). The 3d Wyckoff positions are also kept unspecified, but the intent for these atoms is to stabilize the FCC lattice. Choices of X and Y are also intended to make the X_3Y cage inert such the chemical bonding of the central RH_{11} unit (and therefore its superconducting properties) is preserved. We explore the effects of filling the X and Y positions and hole doping in Fig. S5, finding that the addition of trivalent X atoms typically leads to strong H bonding, bringing the hydro-

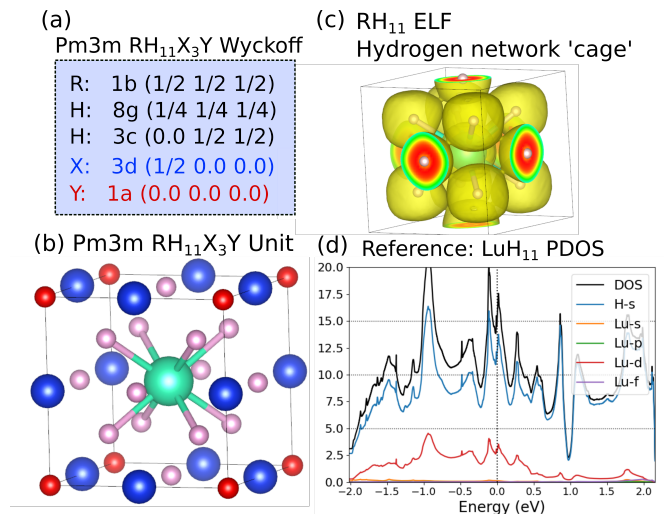


FIG. 2: Proposed $\text{RH}_{11}\text{X}_3\text{Y}$ structures. (a) Structural parameters, (b) Visualization of the $\text{RH}_{11}\text{X}_3\text{Y}$ unit cell, (c) Example electron-localization-function (ELF) of LuH_{11} at an isovalue of 0.55, (d) PDOS of the example LuH_{11} showing metallic hydrogen states dominant at E_F .

gen states far below E_F . Hole-doping and filling $\text{Y}=\text{O}$ both result in hydrogen states dominating the $\text{DOS}(E_F)$, though not at the same magnitude as LuH_{11} [Fig. 2(d)]. These structures are simple enough to perform Eliashberg calculations for T_c , which we do below to further justify the usage of the T_c^{net} estimator for the more complex structures.

We first note that the networking-value T_c estimation formula [Eq. (1)] was found to be within $\pm 60\text{K}$ of isotropic Eliashberg T_c calculations for 300 hydrides [43]. Calculations since then have verified its accuracy at predicting Eliashberg T_c s for CaH_6 (T_c^{Eli} : 236 K, T_c^{net} : 264 K) [44] and $\text{Lu}_4\text{H}_{11}\text{N}$ (T_c^{Eli} : 100 K, T_c^{net} : 99 K) [45]. To gauge the T_c estimation process with our calculations, we estimate using Eq. (1) that $\text{Fm}\bar{3}\text{m LuH}_{10}$ (see Fig. S4) under 150 GPa (alat 4.91 Å) has $T_c \approx 339\text{K}$ compared to the Eliashberg prediction of $T_c = 289\text{K}$ for $\text{Fm}\bar{3}\text{m LuH}_{10}$ under 175 GPa [45]. This shows reasonable agreement between Eq. (1) and isotropic Eliashberg calculations for hydrogen-dense materials. Additionally, our LuH_{11} unit in Fig. 2 (alat 5.21 Å) is estimated to have a T_c^{net} of 266 K. Our hypothesis is that any structure with similar chemical tendencies as these RH_{11} units would have a T_c in a similar range (266 K). We note the similarity to the T_c range reported experimentally for Lu-H-N [36].

1. Example - $\text{Lu}_4\text{H}_{11}\text{O}$

We choose for more extensive calculations the example $\text{Pm}\bar{3}\text{m Lu}_4\text{H}_{11}\text{O}$, shown in Fig. 3. Its DOS near E_F is dominated by hydrogen states, meaning its predicted T_c should be higher than that of $\text{Lu}_4\text{H}_{11}\text{N}$ [45]. We find

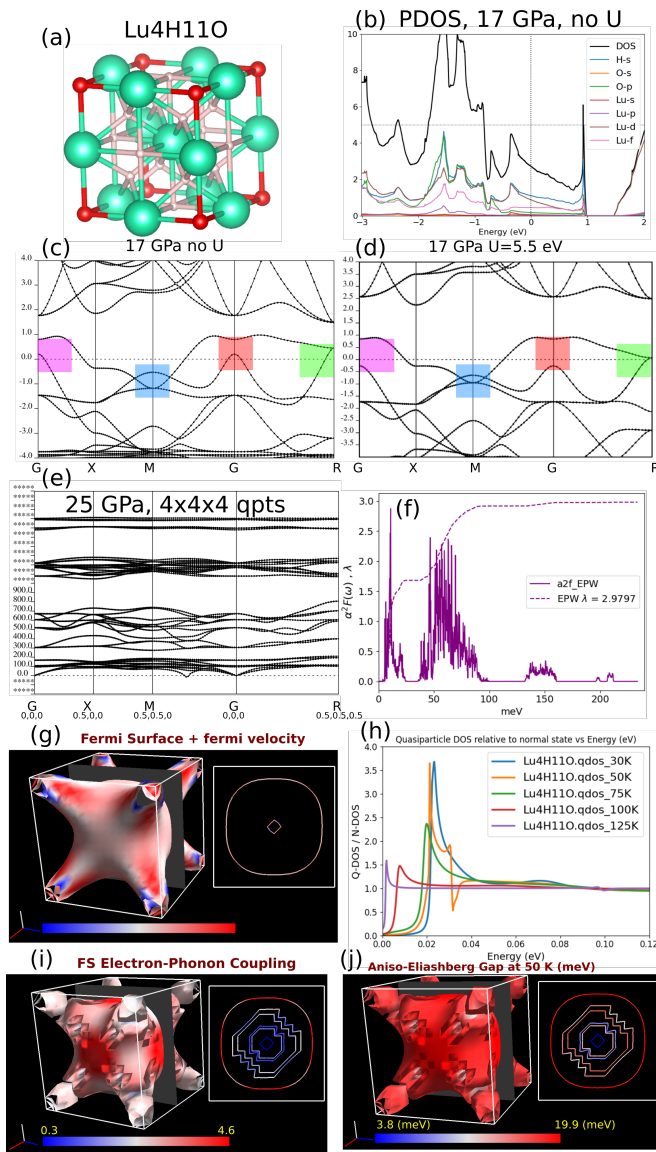


FIG. 3: Electronic, structural, and superconducting properties of Pm3m $\text{Lu}_4\text{H}_{11}\text{O}$. (a) Visualization of the unit cell. (b) PDOS at 17 GPa. (c-d) Band structures with and without +U, with the main differences highlighted. (e) DFPT calculated phonon dispersion, predicting strong softening of quite a few modes. (f) $\alpha^2F(\omega)$ and integrated $\lambda(\omega)$ after convergence studies. (g) Fermi surface, with colors indicating Fermi velocity. (h) Quasiparticle density of states (QDOS) relative to the normal-state DOS. (i) EPC λ_{nk} on the Fermi surface. (j) Superconducting gap Δ_{nk} projected onto the Fermi surface indicating an s-wave gap.

through the ELF that the $\phi_{net}^{crit} = 0.521$. Thus using Eq. (1) the networking value predicted $T_c^{net} = 130$ K (DFT+U quantities bring this T_c up to 140 K). It has regions of flat electron bands 0.9 eV above E_F (around Γ) and 0.36 eV below E_F (around X), and we note increasing correlation effects via DFT+U ($U_d = 5.5$ on Lu)

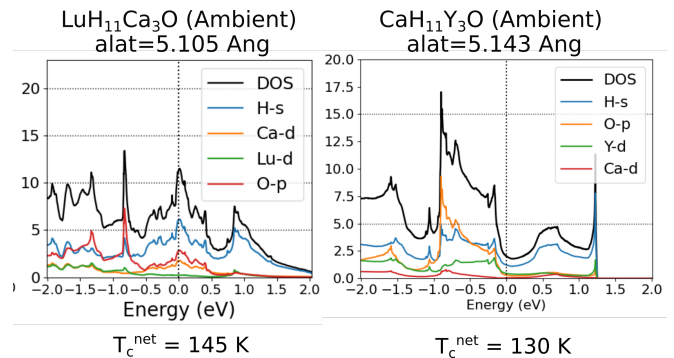


FIG. 4: PDOS and T_c^{net} of two more examples of using the structural formula. (a) $\text{LuH}_{11}\text{Ca}_3\text{O}$, (b) $\text{CaH}_{11}\text{Y}_3\text{O}$.

can induce a Lifshitz transition (Figs. 3(c,d)). Density functional perturbation theory calculations on a $4 \times 4 \times 4$ q-point mesh indicate it is dynamically stable above 25 GPa [Fig. 3(e)], though we note harmonic DFT calculations can overestimate the pressure needed to stabilize the cubic RH_3 compounds by tens of GPa [46]. We used the EPW code [47] to use Wannier functions to interpolate the electron-phonon matrix elements, with k/q meshes of 32^3 and 16^3 . The $\alpha^2F(\omega)$ leads to a large integrated electron-phonon coupling of $\lambda = 3$ [Fig. 3(f)], with an Allen-Dynes T_c of 90 K using $\mu = 0.10$ [31]. We performed anisotropic Eliashberg calculations as implemented in the EPW software [48]. We first show the Fermi surface of $\text{Lu}_4\text{H}_{11}\text{O}$ at 25 GPa [Fig. 3(g)] as well as the quasiparticle DOS in the superconducting state at various temperatures, illustrating the gap closure around 125 K [Fig. 3(h)]. The electron-phonon coupling λ_{nk} and superconducting gap Δ_{nk} at 50 K are projected on the Fermi surface and illustrate a band-dependent s-wave gap structure [Fig. 3(i,j)]. Additional Fermi sheets shown correspond to bands 3 eV below E_F which nevertheless contribute to the electron-phonon coupling. The gap closure around 125 K coincides with the T_c of 130 K predicted by Eq. (1). We note the electron-phonon coupling increases if E_F is reduced by 0.36 eV, coupled with an increase in the size of the strongly-coupled Fermi sheet, which increases T_c slightly and induces a multigap structure (not shown) like LaH_{10} [49]. While YH_3 and Y_2O_3 are known to react to form cubic YH_xO_y [50], it is unclear if synthesizing cubic $\text{Lu}_4\text{H}_{11}\text{O}$ would be possible.

2. Other $\text{RH}_{11}\text{X}_3\text{Y}$ Examples

Eliashberg calculations on $\text{Lu}_4\text{H}_{11}\text{N}$ accounting for quantum ZPM and thermal effects predict a T_c of 100 K [45]. We confirm the T_c predictor [Eq. (1)] predicts 100 K for $\text{Lu}_4\text{H}_{11}\text{N}$ [Fig. 4(a)], agreeing with the Eliashberg calculations [45] despite the former being based purely on electronic properties.

Figure 4 shows the PDOS of two other examples using this first model structure (Fig. 2). Both $\text{LuH}_{11}\text{Ca}_3\text{O}$ and

$\text{CaH}_{11}\text{Y}_3\text{O}$ have dominant $\text{DOS}_H(E_F)$ and end up having similar T_c^{net} despite the almost threefold difference in their total $\text{DOS}_{\text{tot}}(E_F)$. We emphasize this is due to the observation that T_c is not correlated with the total $\text{DOS}(E_F)$ in hydrides, but the relative hydrogen contribution [43].

As boron is known to attain the lowest known oxidation state (B^{5-}), we also explored $\text{Lu}_4\text{H}_{11}\text{B}$ (Fig. S6) and found an interesting flat band near E_F of Lu-d,H-s, and B-p character which remained under relaxation that would likely lead to an instability of some kind. As its predicted T_c^{net} is below 200 K we did not look further at $\text{Lu}_4\text{H}_{11}\text{B}$. We confirm there is no DFT+U dependence for these results (the Fermi level properties do not change).

We note that ScN/YN [51] and YbN/TmN [52] have electronic properties similar to LuN , and could therefore play a similar role as LuN does in $\text{Lu}_8\text{H}_{23}\text{N}$ [53] while potentially stabilizing the FCC lattice. Such alloying for stability purposes is explored in a computational study of quaternary hydrides based on optimal sphere packing ratios [17], finding new dynamically stable alloys confirmed by phonon calculations. Such results can be combined with our analysis to guide choices of X when using the model structure in Fig. 2.

We have established that while the first model structure (Fig. 2) can result in hydrogen-dominant states at E_F , the magnitude of the $\text{DOS}(E_F)$ is not comparable to that of the core RH_{11} unit, and the $\text{DOS}_{H,\text{rel}}(E_F)$ ratio is not typically close to 1, which limits the achievable T_c^{net} (Eq. 1). On the other hand, we can build on the RH_{11} subunit in the small $\text{Pm}\bar{3}\text{m}$ cell, preserving its chemical properties by surrounding it with a charge-inhomogeneous region to form a heterostructure. For example, we can design a supercell in which charge is redirected away from the X_3Y cage surrounding the RH_{11} unit (Fig. 5) and the tetrahedral bonds to the X atoms are weakened, to further emulate RH_{11} .

B. $\text{Fm}\bar{3}\text{m}$ $(\text{RH}_{11})_2\text{X}_6\text{YZ}$ Structure

Starting with the $\text{RH}_{11}\text{X}_3\text{Y}$ structure (Fig. 2), we place atoms next to the 3d-X [indicated by the arrows in Fig. 5(a)] that will redirect the 3d-X electrons. This leads to a picture [Fig. 5(b)] where the RH_{11} metallic hydrogen sublattice is surrounded by a stabilizing auxiliary lattice that isolates its chemistry from the inner RH_{11} units. Such chemically inert regions are typically chosen to be insulating or semiconducting, such as LuN . We visualize and specify a model structure meeting these requirements in Fig. 5(c,d). The blue regions indicate the RH_{11} regions. We use this model first to contextualize our previous work on Lu-H-N [37] before moving on to other examples.

The $\text{Lu}_8\text{H}_{23}\text{N}$ (A) [37] structure can be viewed as a mostly-inert LuN_xH_y cage surrounding metallic units of LuH_{11} that may be locally superconducting and become phase-coherent by tunneling through the LuN_xH_y bar-

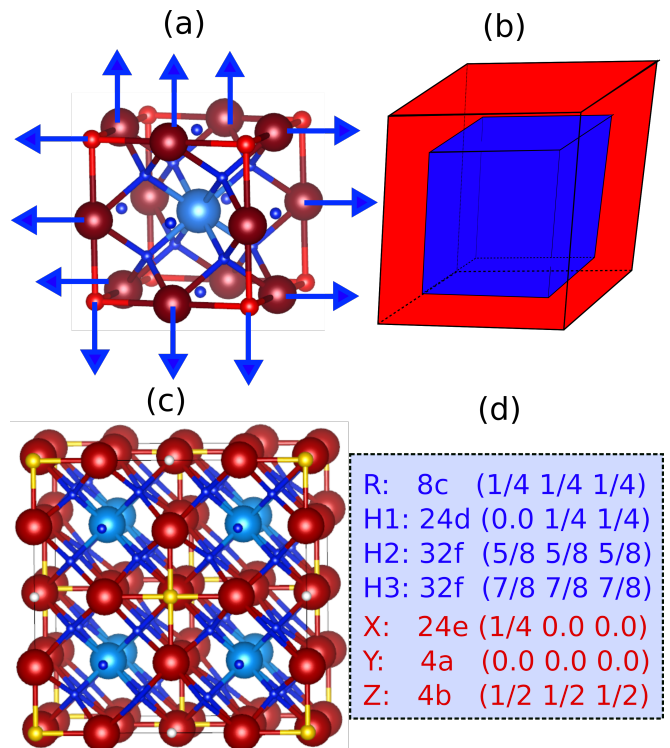


FIG. 5: Strategy for creating the $(\text{RH}_{11})_2\text{X}_6\text{YZ}$ heterostructure that contains RH_{11} units by redirecting the charge of X_3Y layers of the simple model structure (Fig. 2) away from the RH_{11} units. (a) Visualization of extra charge brought by 3d-X atoms being redirected away from the RH_{11} unit. (b) A depiction of an inert X_6YZ shell containing the RH_{11} unit. (c) Plot of $(\text{RH}_{11})_2\text{X}_6\text{YZ}$ using a similar coloring scheme as (b) to further illustrate the concept. (d) The Wyckoff positions of the quaternary heterostructure. The atoms in (c) are colored as: 24e-X (red), 4a-Y (yellow), 4b-Z (white), and RH_{11} units (blue).

riers. This also explains why DFT+U has a large effect on this structure; since LuN requires DFT+U to accurately describe its bandgap of 1.2 eV [52] (becoming semimetallic without U), it is easy to see how the LuN_xH_y cage depends sensitively on U. We also note that the experimental lattice constant of LuN is 4.77 Å, indicating that this LuNH_x shell actually serves an auxiliary purpose of squeezing the inner LuH_{11} unit, providing significant internal pressure. As the $\text{Lu}_8\text{H}_{23}\text{N}$ (A) can be viewed as LuH_{11} units stabilized by LuN_xH_y cages, with a similar $\text{DOS}(E_F)$ [37] as LuH_{11} [Fig. 2(d)], its T_c may be comparable to the original LuH_{11} units, and therefore near 266 K. Using Wannier projections to determine $\text{DOS}_{H,\text{rel}}(E_F)$, its T_c using Eq. (1) is 180 K, though the error bar of 60 K [43] lets it approach the value established experimentally [36].

Our second model structure (Fig. 5) is a heterostructure designed to preserve the hydrogen-dominated band structure near E_F of the core RH_{11} units, with the appropriate choice of X,Y, and Z atoms. It has chemical

formula $(\text{RH}_{11})_2\text{X}_6\text{YZ}$, where R is typically a 3+ atom in the 8c position, X is an atom stabilizing the FCC RH_{11} lattice in the 24e position with $x \approx 0.25$, and Y,Z in the 4a/4b positions ensure the X atoms are inert with respect to the RH_{11} lattice. The hydrogens occupy two 32f positions with $x \approx 0.875$ and $x \approx 0.625$ as well as the 24d positions. Figure S7 shows four examples without relaxing the structure from the parameters given in Fig. 5(d). Their electronic properties suggest a high estimated T_c in the 150-170 K range using Eq. (1). However, these examples are unrelaxed so we do not quantify their properties further.

The parameters in Fig. 5 are used as starting points before a first-principles method (e.g. DFT) is used to further relax the structure. We note the high symmetry of the starting structure prevents certain relaxation pathways due to a cancellation of forces. If one breaks the symmetry of the initial structure, DFT methods which treat nuclei classically tend to move some hydrogen to emulate adsorbed H_2 and become insulating (see Sec. [SI] for more details). However, DFT typically ignores vibrational entropy and zero point energy, which can be a large mitigating effect for such structural deformations in hydrides [54], and we indeed find quantum ZPM and thermal effects anharmonically stabilize the high-symmetry structure for $(\text{LuH}_{11})_2(\text{Lu}_6\text{NH})$ [53]. Similar stabilization of high symmetry structures in hydrides by quantum/thermal effects has been observed [26, 45, 46, 55]. Since such calculations are prohibitively expensive on large supercells, the high symmetry initial structure provided in Fig. 5 serves as a heuristic method to allow DFT relaxations to maintain the high symmetry encouraged by quantum/thermal effects in these systems. We discuss symmetry breaking of the hydrogen later in the context of raising T_c^{net} .

Large imaginary frequencies associated with hydrogen displacements indicate substantial electron-phonon coupling (EPC) [56], and we expect the model structures we provide to commonly have such harmonic instabilities at the DFT level. If quantum/thermal effects nevertheless dynamically stabilize the structure, this provides a pathway other than classical disorder [31] to realize the very large EPC needed for room temperature superconductivity.

1. Example - $(\text{CaH}_{11})_2\text{Sc}_6\text{NH}$

We start with an in-depth look at a particular example of this model structure. Choosing $\text{R}=\text{Ca}$, $\text{X}=\text{Sc}$, $\text{Y}=\text{N}$, and $\text{Z}=\text{H}$, we have $(\text{CaH}_{11})_2\text{Sc}_6\text{NH}$, succinctly $\text{Sc}_{0.75}\text{Ca}_{0.25}\text{H}_{2.875}\text{N}_{0.125}$. These were chosen for stability and superconductivity potential. In terms of stability, the pressure needed to stabilize cubic ScH_3 is predicted to decrease significantly (to about 10 GPa) by 25-33% Ca doping [32]. For superconductivity potential, $\text{CaH}_{n \geq 6}$ has been explored as high-temperature superconductors with CaH_6 achieving a T_c of 215 K [57] and possibly

higher T_c for more hydrogen-rich compounds [58]. Additionally, the idea has been put forward to dope CaH_6 with rare earths to achieve even higher T_c [59, 60]. Finally, these ingredients meet good criteria for the heterostructure: ScN is semiconducting, the Sc atoms will help stabilize the tetrahedral hydrogen in the CaH_{11} unit, and the negative charge on N will tune the bonding effect of the Y atoms, bringing some tetrahedral hydrogen states higher in energy to hybridize with the octahedral hydrogen.

The electronic and phonon properties of $(\text{CaH}_{11})_2\text{Sc}_6\text{NH}$ at 20 GPa is shown in Fig. 6. The PDOS shows multiple hydrogen-dominant peaks at and surrounding E_F , and the bandstructure illustrates various places in the Brillouin Zone where these vHs arise. This electronic structure is reminiscent of the flat bands arising from the hydrogen-based sublattice in $\text{Lu}_8\text{H}_{23}\text{N}$ [53]. The $\phi_{net}^{crit} = 0.585$ in this system, and so the estimated $T_c^{net} = 165$ K. We note if you remove the 4b-H or replace the nitrogen with oxygen, the T_c^{net} rises to 180 K (see Fig. S10). The imaginary phonon frequencies at Γ indicate there may be a hydrogen position instability. To evaluate the likelihood of quantum effects stabilizing this structure against such an instability, we evaluate the anharmonicity of the potential energy surface (PES) associated with displacing the crystal along the corresponding dynamical matrix eigenvector (visualized in the inset). We define the number of hydrogen strongly displaced in the mode to be all hydrogen whose displaced distance is more than $D_{max}/6$, where D_{max} is the maximum distance a hydrogen is displaced. We see the maximum energy gain is 7 meV/hydrogen at an average hydrogen displacement of 0.22 Å. While this energy gain likely increases with DFT+U or when pressure is decreased as in $\text{Lu}_8\text{H}_{23}\text{N}$ [53], the instability is reasonably likely to be cured due to quantum/thermal effects. In Fig. S8 we show examples of ground state densities in the presence of anharmonic potentials; potentials can be surprisingly anharmonic while still favoring a centered wavefunction. We note that as the well is deepened (from i.e. lower pressure) the octahedral hydrogen are expected to transition from high symmetry positions to distorted positions, with a regime in between where spectroscopic signatures are broadened due to quantum ZPM. This interpretation is supported by high-pressure studies of ScH_3 [61].

Supposing the structure does distort, we investigate the electronic properties of the distorted structure and find that the hydrogen DOS has not changed much (consistent with the low energy gain from distortion; also see Fig. S9), yet something remarkable has occurred: the hydrogen displacements have massively improved the hydrogen sublattice connectivity (as measured by ϕ_{iso}^{net} from the ELF), with $\text{H}^{oct}-\text{H}^{tet}$ distances decreasing from 2 Å to 1.74 Å. This is reflected in a large increase of the $\phi_{iso}^{net} = 0.695$. Such H-H distances have recently been observed in other metal hydrides [62, 63]. It is possible that this symmetry-breaking of the octahedral hydrogen

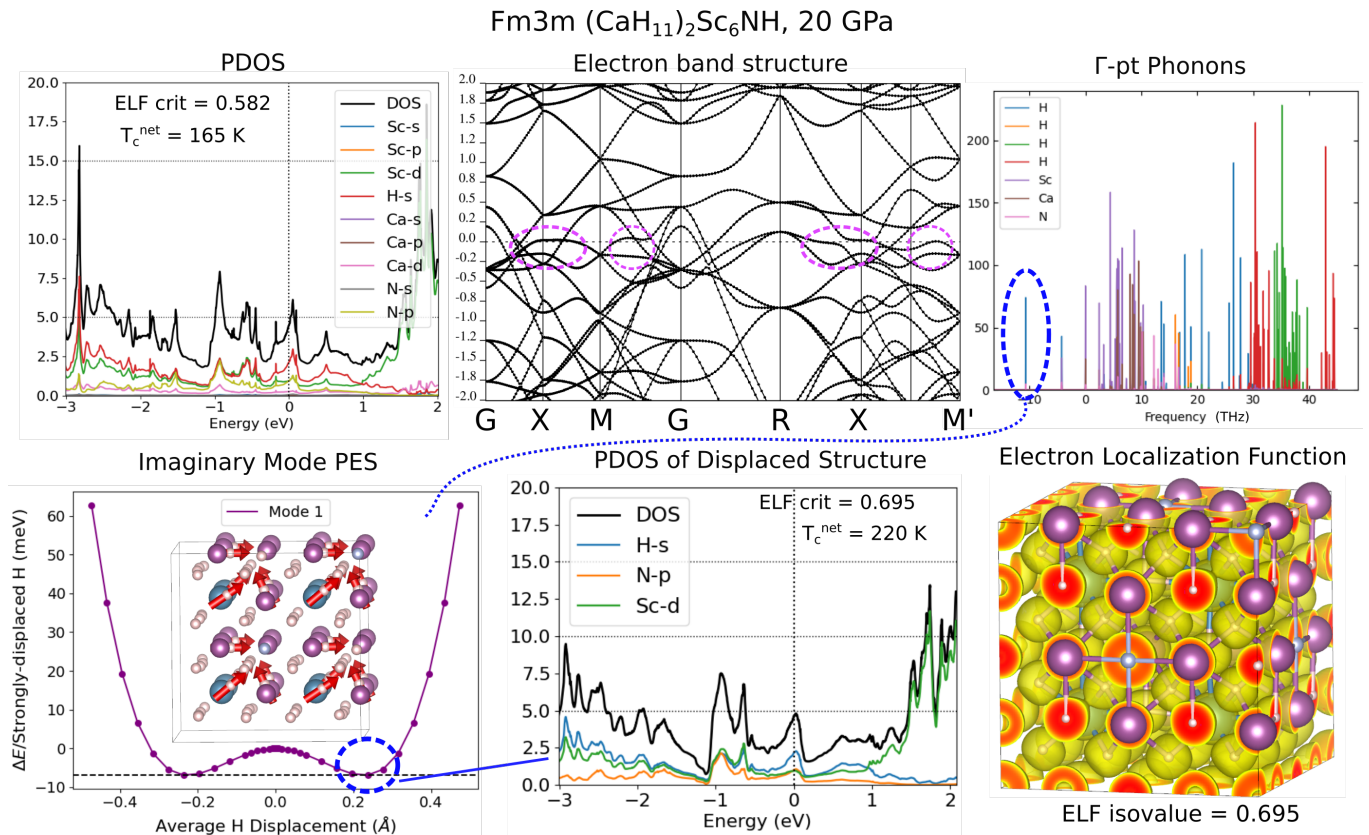


FIG. 6: Electronic and vibrational properties of Sc₆Ca₂H₂₃N at 20 GPa.

enhancing T_c is a more general phenomenon, and may in fact responsible for the high T_c reported in N-doped LuH₃ [36].

Other choices of Y,Z on the electronic properties of (CaH₁₁)₂Sc₆YZ can also enhance T_c^{net} . We show the electronic structure at ambient conditions of a few permutations in Figure S10. At ambient pressures it appears T_c^{net} is highest with Y=N and Z being unoccupied. We note that the Sc_{0.75}Ca_{0.25} system is typically only expected to support a hydrogen content of H_{2.75} in ambient conditions, giving particular importance to this example.

2. Other (RH₁₁)₂X₆YZ Examples

We illustrate two more examples using other elements in Fig. 7. $T_c^{net} = 165$ K in (MgH₁₁)₂Y₆HO and an anomalously high $T_c^{net} = 200$ K in (LaH₁₁)₂Mg₆OH. The electronic properties of these and ten other examples are shown in Fig. S11. We also list the lattice constant used (from PBE-level relaxations), the critical hydrogen networking isovalue ϕ_{iso}^{net} from the ELF, the U-value used (bottom row) and T_c^{net} . We again note T_c^{net} only reproduces T_c^{Eli} within ± 60 K [43]. We order the examples in Fig. S11 by estimated T_c .

We see that all twelve examples in Fig. S11 have hydrogen states dominant at E_F , which correlates with high T_c hydride superconductivity [43]. We note that H_f in Eq.

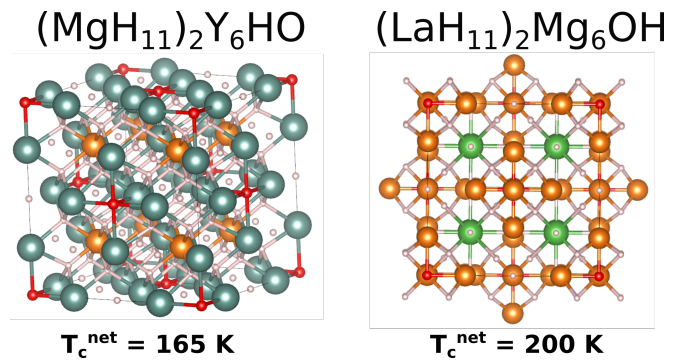


FIG. 7: Structure and predicted T_c^{net} of (MgH₁₁)₂Y₆HO and (LaH₁₁)₂Mg₆OH.

(3) is nearly constant for all of our examples due to the small variance in hydrogen composition. Therefore, the only remaining parameter to try and optimize within this set is ϕ_{iso}^{net} in order to maximize T_c . Using this metric, we find the highest ϕ_{iso}^{net} values in the (RH₁₁)₂(Mg₆OH) systems, with a corresponding networking-value T_c of 200 K. For R=La the high ϕ_{iso}^{net} responsible for this is attributed to hydrogens tetrahedrally oriented with respect to Mg bending away from the oxygen atoms and forming a body-centered cubic hydrogen cage (Fig. S15), with H-H distance 1.964Å between cube edges and 1.692Å between the vertices and the central H atom. Such small

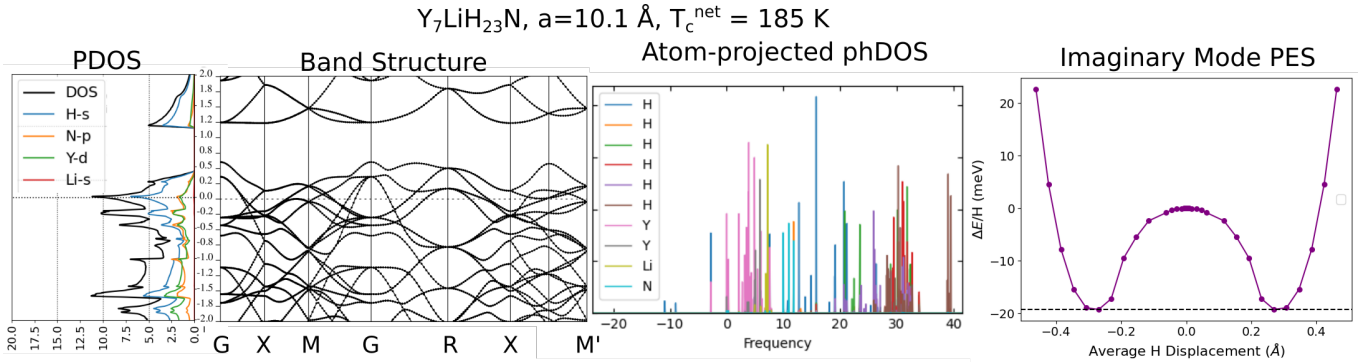


FIG. 8: Properties of $(\text{YLiH}_{22})(\text{Y}_6\text{NH})$, with lattice constant 10.1 \AA . The ϕ_{iso}^{net} increases to 0.61 due to the 24g-H compressing toward the 4d-Y upon Li doping. The networking-value T_c we obtain using the Quantum Espresso projections is 185 K, but increases to 220 K if we use the DOS_H at $E_F+0.3 \text{ eV}$.

H-H distances have also been observed in some intermetallic hydrides [63]. For $R=\text{Sc}$, the hydrogen cubic cage does not form, but the smaller lattice constant appears to make up for it in terms of high ϕ_{iso}^{net} values. Unfortunately, a stability analysis (Sec. SI-A 4 a) indicates $(\text{LaH}_{11})_2\text{Mg}_6\text{OH}$ is dynamically unstable. However, we note the ternary system $(\text{LuH}_{11})_2\text{Lu}_6\text{HN}$ was found to be dynamically stable at ambient pressures when considering quantum effects [53]. We further discuss the stability of compounds with this model structure in Sec. SI-A 4.

Structures with dominant hydrogen states at E_F are often obtained by choosing $R=\text{Sc}/\text{Y}/\text{La}/\text{Lu}$, $X = \text{Li}/\text{Na}/\text{Mg}/\text{Ca}/\text{Sr}/\text{Al}/\text{Ga}/\text{In}$, $Y = \text{H}/\text{O}/\text{S}/\text{N}/\text{P}$, and $Z = \text{H}$. We discuss some common trends in Sec. SI-A 1 and examples where this model structure fails to produce hydrogen-dominant $\text{DOS}(E_F)$ in Sec. SI-A 2. We discuss in Sec. SI-A 3 the interesting case of swapping the role of the R and X atoms resulting again in hydrogen-dominant states at E_F .

While T_c^{net} is generally higher for these examples than our first model structure $\text{RH}_{11}\text{X}_3\text{Y}$, we saw relaxation along instability pathways can in fact raise T_c^{net} through large increases in ϕ_{iso}^{net} . Coupled with a desire to further tune the doping of the rare earth elements, we propose our last model structure, designed to increase ϕ_{iso}^{net} .

C. $\text{F}\bar{4}3\text{m} (\text{R}^1\text{H}_{11})(\text{R}^2\text{H}_{11})\text{X}_6\text{YZ}$ Structure

We propose a structure with symmetry breaking of the 8c-R atoms of our previous model structure, which we capture with the formula $(\text{R}^1\text{H}_{11})(\text{R}^2\text{H}_{11})(\text{X}_6\text{YZ})$, where X is a rare earth atom, and R^1, R^2 are other electron-donating metal atoms (possibly the same as X). The Wyckoff positions are summarized in Fig. 1. The notable change is that this choice purposefully enhances symmetry breaking of the 24d-H positions in the heterostructure. Those hydrogen atoms are observed to shift to either R^1 or R^2 (typically whichever has more valence electrons). In Fig. 1(right) we visualize the symmetry breaking hydrogens (red) as closer towards the 4d- R^2

atoms.

We use this generalization of the $\text{Fm}\bar{3}\text{m} (\text{RH}_{11})_2\text{X}_6\text{YZ}$ to simulate 12.5% doping of ternary $\text{R}_8\text{H}_{23}\text{N}$ structures, which involves choosing $X = \text{R}^2 =$ a rare earth, and R^1 a dopant atom. The doping ratio for this heterostructure is consistent with markedly improved stability properties of FCC RH_3 (see next section).

1. Doping $\text{R}_8\text{H}_{23}\text{N}$

We begin with the interesting electronic structure of $\text{Lu}_8\text{H}_{23}\text{N}$ (A) [37] and investigate replacing Lu with Sc, Y. Cell relaxation was performed and the resulting PDOS and electronic properties are compared in Fig. S17. U-values were chosen by performing DFT+U calculations on the rare earth nitrides and adjusting U_d to match the indirect band gaps to experiment [51]. For $\text{Y}_8\text{H}_{23}\text{N}$, while the flat hydrogen band is still present near E_F , the larger lattice constant results in a smaller ϕ_{iso}^{net} , lowering the estimated T_c . For $\text{Sc}_8\text{H}_{23}\text{N}$ the much smaller lattice constant leads to a higher ϕ_{iso}^{net} but the Sc_d orbitals hybridizing with the Fermi level leads to more charge screening of the negative nitrogen atoms. This brings hydrogen states below E_F and weakens the flatness of the hydrogen band.

Given that doping of YH_3 assists in stabilizing the FCC phase [28, 64–66], we investigate the effects of substituting some $\text{R}=[\text{Sc}, \text{Y}]$ atoms in $\text{R}_8\text{H}_{23}\text{N}$ with alkali and alkali earth atoms. An analysis of doping on the superconducting properties of FCC ScH_3/YH_3 predicts T_c increases up to 90 K [32]. Li-doping of RH_x investigated previously finds T_c up to 242 K at high pressures [67]. Computational studies of the Y-Ca-H system also found high T_c candidates at high pressures [68]. Here we investigate Li, Na, and Mg doping in $\text{Sc}_8\text{H}_{23}\text{N}$, and Li, Mg, and Ca doping in $\text{Y}_8\text{H}_{23}\text{N}$. We start with the parent structure in Fig. 1(right) using $X=\text{Sc}/\text{Y}, \text{R}^1=\text{D}$ (dopant), $\text{R}^2=\text{Sc}/\text{Y}, \text{Y}=\text{H}, \text{Z}=\text{N}$, with the R^1 position occupied by either a dopant $\text{D}=\text{Li}/\text{Mg}/\text{Ca}$ or Sc/Y for lower dopant concentrations.

2. Example: $(YH_{11})(LiH_{11})Y_6HN$

A representative example of the $F\bar{4}3m$ model structure [Fig. 1(right)] is $(YH_{11})(LiH_{11})Y_6HN$ (or $Y_{0.875}Li_{0.125}H_{2.875}N_{0.125}$), which has a lattice constant of 10.1 Å whose stoichiometry is similar to an experimentally stable cubic structure $Y_{0.9}Li_{0.1}H_{2.8}$ [69]. Figure 8 illustrates its electronic and vibrational properties via DFT and frozen phonon calculations [70]. As in previous examples, the $DOS_H(E_F)$ is high and dominant, with contributions from all hydrogen, though the largest contribution is from the 4b-H. The band structure illustrates a propensity of vHs near E_F , as well as flat band regions 0.3 eV below and 1.1 eV above E_F . Though the phonons at ambient reveal imaginary modes, we perform an anharmonicity analysis as done previously for $(CaH_{11})_2Sc_6NH$ (Fig. 6). Here we find the double well expected at this point, though for this compound/pressure it is now deeper than that for $Lu_8H_{23}N$ [53] and $(CaH_{11})_2Sc_6NH$. As designed, the symmetry-broken octahedral hydrogen improve the connectivity of the hydrogen sublattice, increasing ϕ_{iso}^{net} to 0.6 (note our record of ϕ_{iso}^{net} for Y-based hydrides using the previous structure was 0.55; see Fig. S11). This increases T_c to 185 K, which may be increased by pressure and further fine-tuning of doping. Given the deeper double well potential, the structure is quite likely to distort. The distortion features octahedral hydrogen bending towards tetrahedral hydrogen, so it would undoubtedly increase ϕ_{iso}^{net} further. We note the double well's depth goes from -20 meV/hydrogen to -5 meV/hydrogen upon compression by 5 GPa, indicating pressure will likely tune a hydrogen sublattice transition.

3. Other $(R^1H_{11})(R^2H_{11})X_6YZ$ Examples

$(YH_{11})(CaH_{11})Y_6HN$ has a comparatively modest ϕ_{iso}^{net} of 0.56 and T_c^{net} of 180 K [Fig. S12]. We proceed with Sc-based examples, as the reduced lattice constant generally favors high ϕ_{iso}^{net} . Our remaining examples involve doping $Sc_8H_{23}N$ to form $F\bar{4}3m$ $Sc_7[Li,Na,Mg]H_{23}N$. The PDOS, lattice constants, ϕ_{iso}^{net} , and T_c estimates are shown in Fig. 9. Behavior similar to Li-doped $Y_8H_{23}N$ occurs with H shifting towards the 4d-Sc Wyckoff positions. This change coupled with the smaller lattice constant of the FCC ScH_3 parent structure leads to large ϕ_{iso}^{net} due to the robust hydrogen network that forms around the 4d-Sc positions. The T_c estimates of 185-230 K for these structures illustrate the power of combining both nitrogen and alkali metal dopants with this heterostructure design. We did briefly investigate replacing N with S, and found $F\bar{4}3m$ $Sc_7MgH_{23}S$ is insulating but with a high $\phi_{iso}^{net} = 0.655$. Hole-doping, for example with further Mg (perhaps using $Fm\bar{3}m$ $(MgH_{11})_2Sc_6SH$) would create a metal with hydrogen-dominant states. As the highest predicted T_c^{net} so far comes from cubic (Mg,N)-doped ScH_3 , we note Mg and Sc form cubic alloys [71]

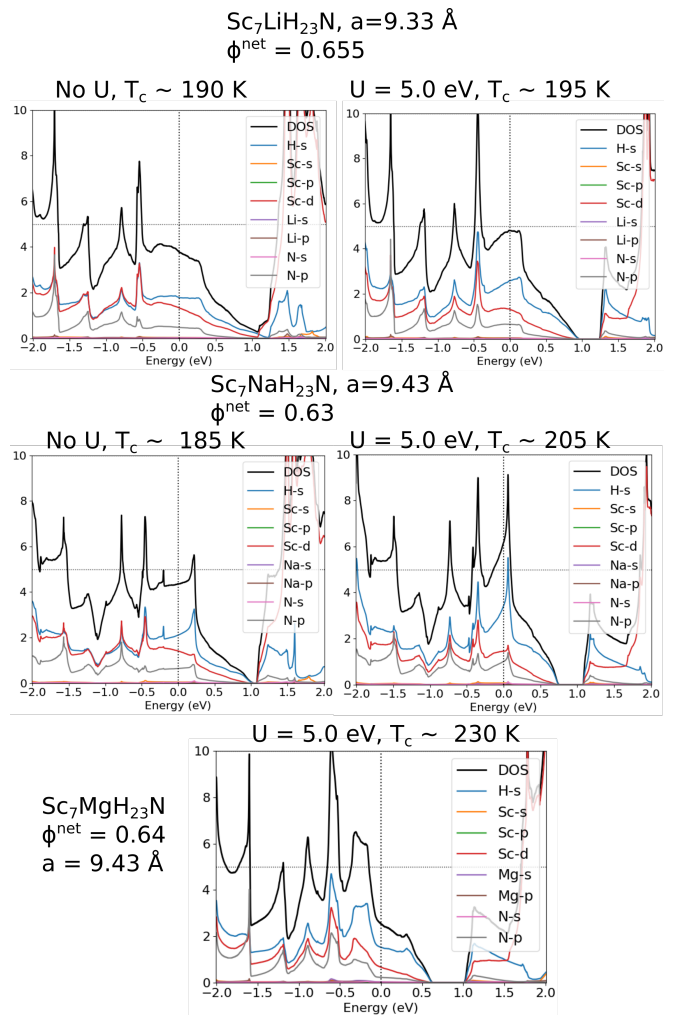


FIG. 9: PDOS, ϕ_{iso}^{net} and T_c estimates of $Sc_7LiH_{23}N$ and $Sc_7NaH_{23}N$ with and without $U_{Sc-d} = 5.0$ eV, and of $Sc_7MgH_{23}N$ with U .

and in fact have been studied as hydrogen storage materials [72, 73].

D. Discussion

In the search for hydride superconductors with very high T_c , a complicating factor is the necessity to include quantum zero-point motion/energy and thermal effects. Without such effects, DFT-based approaches often overestimates structural instabilities for high T_c hydrides. In fact, T_c tends to be highest when the system is closest to structural transitions [74] (and where DFT methods can fail). Another complicating factor for first principles searches is that of metastability; it may prove sufficient for experimental purposes to produce a metastable superconductor (so long as its lifetime is measured in months or years), yet such structures would be discarded in many computational structure searches. We therefore take a different approach and design complex hydride

heterostructures with the intent of producing electronic properties that correlate with high T_c [43]. We use FCC RH_3 as the parent structure, as these structures have high EPC and typically distort away from FCC, but can be stabilized at ambient pressures in a variety of ways [29, 30, 32, 64].

We have proposed three successively more complex model hydride structures with predicted T_c^{net} maximized by having hydrogen-dominant states at E_F and a strongly connected hydrogen sublattice as measured by ϕ_{iso}^{net} . The three models exhibit increased flexibility for tuning stability and T_c relative to binary and ternary systems. Examples within each model structure are candidate high T_c superconductors that are potentially stable near ambient pressure and therefore deserve careful experimental and additional theoretical study.

Compounds based on the first and simplest model structure show moderate promise in producing ternary/quaternary hydride superconductors with T_c in the 100-150 K range. Moreover, we suggest that some of these structures may be stable at ambient pressures. The second and third model structures of quaternary hydrides have enough flexibility to optimize the parameters going into the T_c^{net} estimator, which we use to generate examples with upper estimated T_c^{net} s up to 220-230 K at ambient or near-ambient pressures when accounting for possible hydrogen distortions. We note again T_c^{net} only reproduces T_c from Eliashberg calculations within ± 60 K, so these examples may in fact have T_c exceeding 280 K. As discussed in the SI, it may be necessary to apply a hydrogen gas pressure for some of the realizations of these model structures, but it is unclear from our calculations if only a moderate pressure is needed.

We use the second model structure to better understand $\text{Lu}_8\text{H}_{23}\text{N}$ (A) studied by us previously [37]. As we show elsewhere [53], this structure is dynamically stable at 2.2 GPa when quantum zero-point motion is included, and the flat hydrogen bands are stable against several types of defects, so long as the core LuH_{11} units are left undisturbed. We present a third model structure which in theory can represent complexity higher than quaternary hydrides, we limit ourselves to the quaternary case by analyzing the doping of $[\text{Sc}/\text{Y}]_8\text{H}_{23}\text{N}$ structures. We find that Li,Na,Mg and Ca doping can enhance the estimated T_c of these compounds and the model structure presented here allows hydrogen relaxation to increase ϕ_{iso}^{net} . This doping increases T_c^{net} from $\text{R}_8\text{H}_{23}\text{N}$ by 40-50 K. As it is known experimentally [28, 64] and theoretically [32] that 10-20% alkali/alkali earth doping stabilizes the FCC phases of $[\text{Y},\text{Sc}]\text{H}_3$, we find it likely that these doped $[\text{Sc},\text{Y}]_8\text{H}_{23}\text{N}$ examples with extremely high predicted T_c are synthesizable and stable (perhaps at ≤ 10 GPa for the Sc-based structures). Ball milling[29] and quenching[30] may also play a role in the stabilization of the doped cubic phases discussed here. We note artificial nanostructures with high T_c have been created in cuprates [75] indicating the plausibility of synthesizing

heterostructures following our model structures.

In summary, our model structures constrain the structural/compositional space of doped RH_3 to that of structures with high predicted T_c , which may enable large structure searches (perhaps aided with AI/ML techniques) to efficiently identify quaternary hydrides with the highest T_c . We end by remarking that it is compelling that the highest predicted T_c using our methodology comes from (Mg,N)-doped ScH_3 , which features both Ashcroft's proposal for hydrogen-dominant metallic alloys [22] and Feynman's guess that the highest temperature superconductor would be Sc-based [76].

This research was supported by the NSF (DMR-2104881, R.H.) 303 and DOE-NNSA through the Chicago/DOE Alliance Center (DE-NA0003975; A.D., R.H.), and NSF SI2-SSE Grant 1740112 (H.P.).

- [1] H. K. Onnes, The superconductivity of mercury, *Comm. Phys. Lab. Univ. Leiden* **122**, 124 (1911).
- [2] N. W. Ashcroft, Metallic hydrogen: A high-temperature superconductor?, *Phys. Rev. Lett.* **21**, 1748 (1968).
- [3] V. L. Ginzburg, The problem of high-temperature superconductivity, *Annual Review of Materials Science* **2**, 663 (1972).
- [4] M. Somayazulu, M. Ahart, A. K. Mishra, Z. M. Geballe, M. Baldini, Y. Meng, V. V. Struzhkin, and R. J. Hemley, Evidence for superconductivity above 260 K in lanthanum superhydride at megabar pressures, *Phys. Rev. Lett.* **122**, 027001 (2019).
- [5] A. Drozdov, P. Kong, V. Minkov, S. Besedin, M. Kuzovnikov, S. Mozaffari, L. Balicas, F. Balakirev, D. Graf, V. Prakapenka, *et al.*, Superconductivity at 250 K in lanthanum hydride under high pressures, *Nature* **569**, 528 (2019).
- [6] E. Snider, N. Dasenbrock-Gammon, R. McBride, X. Wang, N. Meyers, K. V. Lawler, E. Zurek, A. Salamat, and R. P. Dias, Synthesis of yttrium superhydride superconductor with a transition temperature up to 262 K by catalytic hydrogenation at high pressures, *Phys. Rev. Lett.* **126**, 117003 (2021).
- [7] P. Kong, V. S. Minkov, M. A. Kuzovnikov, A. P. Drozdov, S. P. Besedin, S. Mozaffari, L. Balicas, F. F. Balakirev, V. B. Prakapenka, S. Chariton, *et al.*, Superconductivity up to 243 K in the yttrium-hydrogen system under high pressure, *Nature Comm.* **12**, 5075 (2021).
- [8] I. A. Troyan, D. V. Semenov, A. G. Kvashnin, A. V. Sadakov, O. A. Sobolevskiy, V. M. Pudalov, A. G. Ivanova, V. B. Prakapenka, E. Greenberg, A. G. Gavriliuk, *et al.*, Anomalous high-temperature superconductivity in YH_6 , *Adv. Mater.* **33**, 2006832 (2021).
- [9] K. P. Hilleke and E. Zurek, Tuning chemical precompression: Theoretical design and crystal chemistry of novel hydrides in the quest for warm and light superconductivity at ambient pressures, *J. Appl. Phys.* **131**, 070901 (2022).
- [10] H. Liu, I. I. Naumov, R. Hoffmann, N. W. Ashcroft, and R. J. Hemley, Potential high- T_c superconducting lanthanum and yttrium hydrides at high pressure, *Proc. Nat. Acad. Sci.* **114**, 6990 (2017).
- [11] F. Peng, Y. Sun, C. J. Pickard, R. J. Needs, Q. Wu, and Y. Ma, Hydrogen clathrate structures in rare earth hydrides at high pressures: possible route to room-temperature superconductivity, *Phys. Rev. Lett.* **119**, 107001 (2017).
- [12] D. V. Semenov, I. A. Troyan, A. G. Ivanova, A. G. Kvashnin, I. A. Kruglov, M. Hanfland, A. V. Sadakov, O. A. Sobolevskiy, K. S. Pervakov, I. S. Lyubutin, *et al.*, Superconductivity at 253 K in lanthanum–yttrium ternary hydrides, *Materials Today* **48**, 18 (2021).
- [13] Y. Song, J. Bi, Y. Nakamoto, K. Shimizu, H. Liu, B. Zou, G. Liu, H. Wang, and Y. Ma, Stoichiometric ternary superhydride LaBeH_8 as a new template for high-temperature superconductivity at 110 K under 80 GPa, *Phys. Rev. Lett.* **130**, 266001 (2023).
- [14] S. Chen, Y. Qian, X. Huang, W. Chen, J. Guo, K. Zhang, J. Zhang, H. Yuan, and T. Cui, High-temperature superconductivity up to 223 K in the Al stabilized metastable hexagonal lanthanum superhydride, *National Science Review* **11**, nwad107 (2024).
- [15] X. Liang, A. Bergara, X. Wei, X. Song, L. Wang, R. Sun, H. Liu, R. J. Hemley, L. Wang, G. Gao, *et al.*, Prediction of high- T_c superconductivity in ternary lanthanum borohydrides, *Phys. Rev. B* **104**, 134501 (2021).
- [16] Y. Sun, S. Sun, X. Zhong, and H. Liu, Prediction for high superconducting ternary hydrides below megabar pressure, *J. Physics: Condensed Matter* **34**, 505404 (2022).
- [17] R. Koshiji, M. Fukuda, M. Kawamura, and T. Ozaki, Prediction of quaternary hydrides based on densest ternary sphere packings, *Phys. Rev. Mater.* **6**, 114802 (2022).
- [18] K. Dolui, L. J. Conway, C. Heil, T. A. Strobel, R. Prasankumar, and C. J. Pickard, Feasible route to high-temperature ambient-pressure hydride superconductivity, *arXiv preprint arXiv:2310.07562* (2023).
- [19] G. M. Shutov, D. V. Semenov, I. A. Kruglov, and A. R. Oganov, Ternary superconducting hydrides in the lm-h system, *Mater. Today Phys.* **40**, 101300 (2024).
- [20] F. Zheng, Z. Zhang, Z. Wu, S. Wu, Q. Lin, R. Wang, Y. Fang, C.-Z. Wang, V. Antropov, Y. Sun, *et al.*, Prediction of ambient pressure superconductivity in cubic ternary hydrides with MH_6 octahedra, *Mater. Today Phys.*, 101374 (2024).
- [21] X. Liang, X. Wei, E. Zurek, A. Bergara, P. Li, G. Gao, and Y. Tian, Design of high-temperature superconductors at moderate pressures by alloying AlH_3 or GaH_3 , *Matter Radiat. at Extremes* **9** (2024).
- [22] N. W. Ashcroft, Hydrogen dominant metallic alloys: high temperature superconductors?, *Phys. Rev. Lett.* **92**, 187002 (2004).
- [23] M. Shao, S. Chen, W. Chen, K. Zhang, X. Huang, and T. Cui, Superconducting ScH_3 and LuH_3 at megabar pressures, *Inorg. Chem.* **60**, 15330 (2021).
- [24] T. Lu, S. Meng, and M. Liu, Electron-phonon interactions in LuH_2 , LuH_3 , and LuN , *arXiv preprint arXiv:2304.06726* (2023).
- [25] P. P. Ferreira, L. J. Conway, A. Cucciari, S. Di Cataldo, F. Giannessi, E. Kogler, L. T. Eleno, C. J. Pickard, C. Heil, and L. Boeri, Search for ambient superconductivity in the Lu-N-H system, *Nature Comm.* **14** (2023).
- [26] D. Dangić, P. Garcia-Goicelaya, Y.-W. Fang, J. Ibanez-Azpiroz, and I. Errea, Ab initio study of the structural, vibrational, and optical properties of potential parent structures of nitrogen-doped lutetium hydride, *Phys. Rev. B* **108**, 064517 (2023).
- [27] A. Meninno and I. Errea, Ab initio study of metastable occupation of tetrahedral sites in palladium hydrides and its impact on superconductivity, *Phys. Rev. B* **107**, 024504 (2023).
- [28] S. Van der Molen, D. Nagengast, A. Van Gogh, J. Kalkman, E. S. Kooij, J. Rector, and R. Griessen, Insulating fcc $\text{YH}_{3-\delta}$ stabilized by MgH_2 , *Phys. Rev. B* **63**, 235116 (2001).
- [29] R. Kataoka, T. Kojima, K. Tada, M. Kitta, N. Takeichi, K. Sakaki, M. Nozaki, T. Kimura, and A. Kamegawa, Face-centered-cubic yttrium trihydride high-pressure phase stabilized at ambient pressures by mechanical milling, *Materialia* **15**, 100956 (2021).
- [30] R. Kataoka, N. Taguchi, M. Kitta, N. Takeichi, R. Ut-

- sumi, H. Saitoh, M. Nozaki, and A. Kamegawa, The origin of the highly crystallized face-centered cubic yh3 high-pressure phase when quenched to ambient condition, *Materials Today Comm.* **31**, 103265 (2022).
- [31] P. Allen and R. Dynes, Superconductivity at very strong coupling, *J. Phys. C: Solid State Physics* **8**, L158 (1975).
- [32] S. Villa-Cortés and O. De la Peña-Seaman, Superconductivity on sch3 and yh3 hydrides: Effects of applied pressure in combination with electron-and hole-doping on the electron-phonon coupling properties, *Chinese J. Physics* **77**, 2333 (2022).
- [33] Z. Ouyang, M. Gao, and Z.-Y. Lu, Superconductivity at ambient pressure in hole-doped LuH₃, arXiv preprint arXiv:2306.13981 (2023).
- [34] X. Hao, X. Wei, H. Liu, X. Song, R. Sun, G. Gao, and Y. Tian, First-principles calculations on structural stability and electronic properties of nitrogen-doped lutetium hydrides under pressure, *Physical Review Research* **5**, 043238 (2023).
- [35] N. Dasenbrock-Gammon, E. Snider, R. McBride, H. Pasan, D. Durkee, N. Khalvashi-Sutter, S. Munasinghe, S. E. Dissanayake, K. V. Lawler, A. Salamat, *et al.*, Evidence of near-ambient superconductivity in a N-doped lutetium hydride, *Nature* **615**, 244 (2023).
- [36] N. P. Salke, A. C. Mark, M. Ahart, and R. J. Hemley, Evidence for near ambient superconductivity in the lu-nh system, arXiv preprint arXiv:2306.06301 (2023).
- [37] A. Denchfield, H. Park, and R. J. Hemley, Electronic structure of nitrogen-doped lutetium hydrides, *Phys. Rev. Mater.* **8**, L021801 (2024).
- [38] W. Kohn and L. J. Sham, Self-consistent equations including exchange and correlation effects, *Physical Review* **140**, A1133 (1965).
- [39] P. Giannozzi, S. Baroni, N. Bonini, M. Calandra, R. Car, C. Cavazzoni, D. Ceresoli, G. L. Chiarotti, M. Cococcioni, I. Dabo, *et al.*, Quantum espresso: a modular and open-source software project for quantum simulations of materials, *J. Physics: Cond. Matter* **21**, 395502 (2009).
- [40] P. Giannozzi, O. Andreussi, T. Brumme, O. Bunau, M. B. Nardelli, M. Calandra, R. Car, C. Cavazzoni, D. Ceresoli, M. Cococcioni, *et al.*, Advanced capabilities for materials modelling with quantum espresso, *J. Physics: Cond. Matter* **29**, 465901 (2017).
- [41] Y.-C. Wang, Z.-H. Chen, and H. Jiang, The local projection in the density functional theory plus U approach: A critical assessment, *J. Chem. Phys.* **144**, 144106 (2016).
- [42] S. A. Tolba, K. M. Gameel, B. A. Ali, H. A. Almossalami, and N. K. Allam, The DFT+U: Approaches, accuracy, and applications, *Density Functional Calculations-Recent Progresses of Theory and Application*, edited by G. Yang, Chapter 1 **1**, 5772 (2018).
- [43] F. Belli, T. Novoa, J. Contreras-Garcia, and I. Errea, Strong correlation between electronic bonding network and critical temperature in hydrogen-based superconductors, *Nature Comm.* **12**, 5381 (2021).
- [44] H. Jeon, C. Wang, S. Liu, J. M. Bok, Y. Bang, and J.-H. Cho, Electron-phonon coupling and superconductivity in an alkaline earth hydride cah6 at high pressures, *New J. Physics* **24**, 083048 (2022).
- [45] Y.-W. Fang, D. Dangi'c, and I. Errea, Assessing the feasibility of near-ambient conditions superconductivity in the lu-nh system, arXiv preprint arXiv:2307.10699 (2023).
- [46] R. Lucrezi, P. P. Ferreira, M. Aichhorn, and C. Heil, Temperature and quantum anharmonic lattice effects on stability and superconductivity in lutetium trihydride, *Nature Comm.* **15**, 441 (2024).
- [47] S. Poncé, E. R. Margine, C. Verdi, and F. Giustino, Epw: Electron-phonon coupling, transport and superconducting properties using maximally localized wannier functions, *Computer Physics Comm.* **209**, 116 (2016).
- [48] E. R. Margine and F. Giustino, Anisotropic migdal-eliashberg theory using wannier functions, *Phys. Rev. B* **87**, 024505 (2013).
- [49] C. Wang, S. Yi, and J.-H. Cho, Multiband nature of room-temperature superconductivity in lah 10 at high pressure, *Phys. Rev. B* **101**, 104506 (2020).
- [50] N. Zapp, H. Auer, and H. Kohlmann, Yho, an air-stable ionic hydride, *Inorganic Chemistry* **58**, 14635 (2019).
- [51] J. Liu, X.-B. Li, H. Zhang, W.-J. Yin, H.-B. Zhang, P. Peng, and L.-M. Liu, Electronic structures and optical properties of two-dimensional scn and yn nanosheets, *J. Appl. Phys.* **115** (2014).
- [52] M. Topsakal and R. Wentzcovitch, Accurate projected augmented wave (paw) datasets for rare-earth elements (re= la-lu), *Computational Materials Science* **95**, 263 (2014).
- [53] A. Denchfield, H. Park, and R. Hemley, TBD (In Preparation).
- [54] X. Wang and H. Chen, Large entropy derived from low-frequency vibrations and its implications for hydrogen storage, *Appl. Phys. Lett.* **112** (2018).
- [55] L. Monacelli, R. Bianco, M. Cherubini, M. Calandra, I. Errea, and F. Mauri, The stochastic self-consistent harmonic approximation: calculating vibrational properties of materials with full quantum and anharmonic effects, *J. Phys.: Condens. Matt.* **33**, 363001 (2021).
- [56] F. Giustino, Electron-phonon interactions from first principles, *Reviews of Modern Physics* **89**, 015003 (2017).
- [57] L. Ma, K. Wang, Y. Xie, X. Yang, Y. Wang, M. Zhou, H. Liu, X. Yu, Y. Zhao, H. Wang, *et al.*, High-temperature superconducting phase in clathrate calcium hydride cah 6 up to 215 k at a pressure of 172 gpa, *Physical Review Letters* **128**, 167001 (2022).
- [58] Z. Shao, D. Duan, Y. Ma, H. Yu, H. Song, H. Xie, D. Li, F. Tian, B. Liu, and T. Cui, Unique phase diagram and superconductivity of calcium hydrides at high pressures, *Inorganic chemistry* **58**, 2558 (2019).
- [59] K. Yang, H. Sun, H. Chen, L. Chen, B. Li, and W. Lu, Stable structures and superconducting properties of cala-h compounds under pressure, *J. Phys. Condens. Matter* **34**, 355401 (2022).
- [60] D. Papaconstantopoulos, M. Mehl, and E. Economou, High-temperature superconductivity in the ca-sc-h system, *Phys. Rev. B* **108**, 224508 (2023).
- [61] T. Kume, H. Ohura, T. Takeichi, A. Ohmura, A. Machida, T. Watanuki, K. Aoki, S. Sasaki, H. Shimizu, and K. Takemura, High-pressure study of ScH₃: Raman, infrared, and visible absorption spectroscopy, *Phys. Rev. B* **84**, 064132 (2011).
- [62] V. E. Antonov, V. K. Fedotov, A. S. Ivanov, A. I. Kolesnikov, M. A. Kuzovnikov, M. Tkacz, and V. A. Yartys, Lattice dynamics of high-pressure hydrides studied by inelastic neutron scattering, *J. Alloys*

- Compd. **905**, 164208 (2022).
- [63] R. A. Klein, R. Balderas-Xicohténcatl, J. P. Maehlen, T. J. Udovic, C. M. Brown, R. Delaplane, Y. Cheng, R. V. Denys, A. J. Ramirez-Cuesta, and V. A. Yartys, Neutron vibrational spectroscopic evidence for short H-H contacts in the $R\text{NiInH}_{1.4;1.6}$ ($R = \text{Ce, La}$) metal hydride, *J. Alloys and Compounds* **894**, 162381 (2022).
- [64] R. Kataoka, T. Kimura, K. Sakaki, M. Nozaki, T. Kojima, K. Ikeda, T. Otomo, N. Takeichi, and A. Kamegawa, Facile synthesis of lih-stabilized face-centered-cubic yh_3 high-pressure phase by ball milling process, *Inorganic chemistry* **58**, 13102 (2019).
- [65] R. Kataoka, M. Nozaki, T. Kimura, K. Sakaki, T. Kojima, K. Ikeda, T. Otomo, N. Takeichi, and A. Kamegawa, Zirconium hydride-stabilized yttrium hydride (zsy): Stabilization of a face-centered cubic yh_3 phase by zr substitution, *J. Alloys and Compounds* **851**, 156071 (2021).
- [66] A.-M. Carsteanu, M. Rode, D. Zur, J. Schoenes, A. Borgschulte, and R. Westerwaal, Distortion of the fcc lattice in superstoichiometric $\beta\text{-yh}_{2+\delta}$ and cubic $\text{yh}_{3-\eta}$ thin films, *J. Alloys Compd.* **404-406**, 82 (2005), proceedings of the 9th International Symposium on Metal-Hydrogen Systems, Fundamentals and Applications (MH2004).
- [67] Y. Sun, Y. Wang, X. Zhong, Y. Xie, and H. Liu, High-temperature superconducting ternary Li-R-H superhydrides at high pressures ($R = \text{Sc, Y, La}$), *Phys. Rev. B* **106**, 024519 (2022).
- [68] X. Liang, A. Bergara, L. Wang, B. Wen, Z. Zhao, X.-F. Zhou, J. He, G. Gao, and Y. Tian, Potential high- t_c superconductivity in CaYH_{12} under pressure, *Phys. Rev. B* **99**, 100505 (2019).
- [69] R. Kataoka, T. Kimura, N. Takeichi, and A. Kamegawa, Stabilization of face-centered cubic high-pressure phase of REH_3 ($\text{RE} = \text{Y, Gd, Dy}$) at ambient pressure by alkali or alkaline-earth substitution, *Inorganic Chemistry* **57**, 4686 (2018).
- [70] A. Togo, First-principles phonon calculations with phonopy and phono3py, *J. Physical Society of Japan* **92**, 012001 (2023).
- [71] O. t. Schob and E. Parthé, Ab compounds with sc, y and rare earth metals. i. scandium and yttrium compounds with crb and cscl structure, *Acta Crystallographica* **19**, 214 (1965).
- [72] W. Kalisvaart, R. Niessen, and P. Notten, Electrochemical hydrogen storage in mgsc alloys: A comparative study between thin films and bulk materials, *J. Alloys Compd.* **417**, 280 (2006).
- [73] S. Al, N. Cavdar, and N. Arikan, Computational evaluation of comprehensive properties of mgx_3h_8 ($x = \text{sc, ti}$ and zr) as effective solid state hydrogen storage materials, *J. Energy Storage* **80**, 110402 (2024).
- [74] Y. Quan, S. S. Ghosh, and W. E. Pickett, Compressed hydrides as metallic hydrogen superconductors, *Phys. Rev. B* **100**, 184505 (2019).
- [75] G. Balestrino, S. Lavanga, P. Medaglia, P. Orgiani, and A. Tebano, Interlayer coupling in ultrathin high- t_c artificial structures, *Phys. Rev. B* **64**, 020506 (2001).
- [76] D. Goodstein and J. Goodstein, Richard feynman and the history of superconductivity, *Physics in Perspective* **2**, 30 (2000).
- [77] Denchfield, A, et al, In Preparation.
- [78] T. Yamamoto, K. Kaminaga, D. Saito, D. Oka, and T. Fukumura, High electron mobility with significant spin-orbit coupling in rock-salt YbO epitaxial thin film, *Appl. Phys. Lett.* **114** (2019).
- [79] Denchfield, A, et al; In Preparation.
- [80] P. Fischer, W. Halg, L. Schlapbach, and K. Yvon, Neutron and x-ray diffraction investigation of deuterium storage in La_7Ni_3 , *J. Less Common Metals* **60**, 1 (1978).
- [81] T. Ito, B. Beaudry, K. Gschneidner Jr, and T. Takeshita, Phase transitions and polymorphism in $\text{LaH}_{3.0}$ and $\text{LaD}_{3.0}$ at low temperatures, *Phys. Rev. B* **27**, 2830 (1983).
- [82] K. Kai, K. Gschneidner Jr, B. Beaudry, and D. Peterson, Heat capacities of LaD_x and LaH_x ($1.9 < x < 3.0$) from 1 to 300 K, *Phys. Rev. B* **40**, 6591 (1989).
- [83] G. Majer, U. Kaess, and R. Barnes, Model-independent measurements of hydrogen diffusivity in the lanthanum dihydride-trihydride system, *Phys. Rev. Lett.* **83**, 340 (1999).
- [84] L. Ouyang, F. Qin, and M. Zhu, The hydrogen storage behavior of Mg_3La and $\text{Mg}_3\text{LaNi}_{0.1}$, *Scripta materialia* **55**, 1075 (2006).
- [85] A. Peles and C. G. Van de Walle, Role of charged defects and impurities in kinetics of hydrogen storage materials: A first-principles study, *Phys. Rev. B* **76**, 214101 (2007).
- [86] M. S. Salman, C. Prathana, Q. Lai, T. Wang, N. Rambhujun, K. Srivastava, and K.-F. Aguey-Zinsou, Catalysis in solid hydrogen storage: Recent advances, challenges, and perspectives, *Energy Technology* **10**, 2200433 (2022).
- [87] A. Gross and M. Scheffler, Role of zero-point effects in catalytic reactions involving hydrogen, *J. Vacuum Science & Technology A: Vacuum, Surfaces, and Films* **15**, 1624 (1997).
- [88] C. Boonchot, P. Tsuppayakorn-Aek, U. Pinsook, and T. Bovornratanaraks, Stability and electronic structure of magnesium hydride and magnesium deuteride under high pressure, in *J. Physics: Conference Series*, Vol. 2145 (IOP Publishing, 2021) p. 012026.
- [89] A. V. Chubukov, A. Abanov, I. Esterlis, and S. A. Kivelson, Eliashberg theory of phonon-mediated superconductivity—when it is valid and how it breaks down, *Annals of Physics* **417**, 168190 (2020).
- [90] R. Lucrezi, E. Kogler, S. Di Cataldo, M. Aichhorn, L. Boeri, and C. Heil, Quantum lattice dynamics and their importance in ternary superhydride clathrates, *Comm. Physics* **6**, 298 (2023).
- [91] Denchfield, A, et al; In Preparation.
- [92] G. Prandini, A. Marrazzo, I. E. Castelli, N. Mounet, and N. Marzari, Precision and efficiency in solid-state pseudopotential calculations, *npj Comp. Mater.* **4**, 1 (2018).
- [93] A. Dal Corso, Pseudopotentials periodic table: From H to Pu, *Comp. Mater. Sci.* **95**, 337 (2014).
- [94] M. Schlipf, M. Betzinger, C. Friedrich, M. Ležaić, and S. Blügel, Hse hybrid functional within the flapw method and its application to gdn, *Phys. Rev. B* **84**, 125142 (2011).
- [95] M. Kawamura, Y. Gohda, and S. Tsuneyuki, Improved tetrahedron method for the brillouin-zone integration applicable to response functions, *Phys. Rev. B* **89**, 094515 (2014).
- [96] K. Momma and F. Izumi, Vesta 3 for three-dimensional visualization of crystal, volumetric and morphology data, *J. Appl. Crystallography* **44**, 1272 (2011).
- [97] D. Chakraborty, K. Berland, and T. Thonhauser, Next-

- generation nonlocal van der waals density functional, *J. Chem. Theory and Comput.* **16**, 5893 (2020).
- [98] J. P. Perdew, K. Burke, and M. Ernzerhof, Generalized gradient approximation made simple, *Phys. Rev. Lett.* **77**, 3865 (1996).
- [99] S. Gariglio, N. Reyren, A. Caviglia, and J.-M. Triscone, Superconductivity at the LaAlO₃/SrTiO₃ interface, *J. Phys.s: Condens. Matt.* **21**, 164213 (2009).
- [100] P. Zubko, S. Gariglio, M. Gabay, P. Ghosez, and J.-M. Triscone, Interface physics in complex oxide heterostructures, *Annu. Rev. Condens. Matter Phys.* **2**, 141 (2011).
- [101] C. Liu, X. Yan, D. Jin, Y. Ma, H.-W. Hsiao, Y. Lin, T. M. Bretz-Sullivan, X. Zhou, J. Pearson, B. Fisher, *et al.*, Two-dimensional superconductivity and anisotropic transport at KTaO₃ (111) interfaces, *Science* **371**, 716 (2021).
- [102] D.-H. Lee, Routes to high-temperature superconductivity: a lesson from FeSe/SrTiO₃, *Annu. Rev. Condens. Matter Phys.* **9**, 261 (2018).
- [103] N. Bergeal, X. Grisson, J. Lesueur, G. Faini, M. Aprili, and J. Contour, High-quality planar high-*t_c* josephson junctions, *Applied physics letters* **87** (2005).
- [104] I. Bozovic, G. Logvenov, M. Verhoeven, P. Caputo, E. Goldobin, and M. Beasley, Giant proximity effect in cuprate superconductors, *Phys. Rev. Lett.* **93**, 157002 (2004).
- [105] V. Kresin, Y. Ovchinnikov, and S. Wolf, “giant” josephson proximity effect, *Applied physics letters* **83**, 722 (2003).

SUPPLEMENTAL INFORMATION

Designing Quaternary Hydrides with Potential High T_c Superconductivity

Adam Denchfield,¹ Hyowon Park,^{1,2} and Russell J. Hemley^{1,3,4}

¹*Department of Physics, University of Illinois Chicago, Chicago, Illinois 60607, USA*

²*Materials Science Division, Argonne National Laboratory, Lemont, Illinois 60439, USA*

³*Department of Chemistry, University of Illinois Chicago, Chicago, Illinois 60607, USA*

⁴*Department of Earth and Environmental Sciences,
University of Illinois Chicago, Chicago, Illinois 60607, USA*

(Dated: March 4th, 2024)

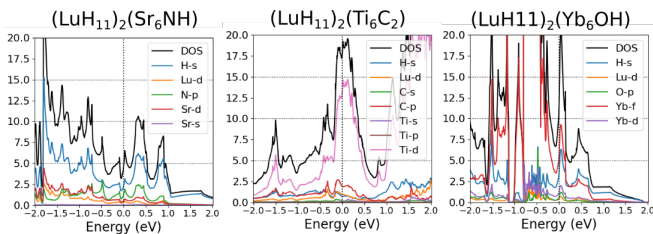


FIG. S1: PDOS calculated for three examples using $R=\text{Lu}$. One uses $X=\text{Sr}$, $Y=\text{N}$, $Z=\text{H}$ (left), another uses $X=\text{Ti}$, $Y=Z=\text{C}$ (middle), and the last uses $X=\text{Yb}$, $Y=\text{O}$, $Z=\text{H}$ (right).

Appendix SI-A: Additional Information about Model Structure $(\text{RH}_{11})_2\text{X}_6\text{YZ}$

1. DOS Trends & DFT+U Dependence

A trend can be seen for some of the compositions seen in Figures S11 and S14. There is a common shape to the DOS near E_F , highlighted for four examples in Fig. S13. This is encouraging, as it illustrates the chemistry is similar among different compositions. In particular, this electronic structure is associated with the quantum interference caused by the Lewis base (N,O,S,P), as shown in our work on $\text{Lu}_8\text{H}_{23}\text{N}$ [77].

Out of the examples shown, we found only significant dependence on U for the cases involving rare earth nitride/oxide units in the auxiliary cages of the model structures. This is expected, as for example the rare earth nitrides' semiconducting properties severely change with U using PBE with PAW pseudopotentials [52], going from a bandgap of ~ 0.1 eV to ~ 1 eV (the latter being the experimental bandgap).

2. Counterexamples

It is important to understand that the model structures discussed in the main text do not guarantee a hydrogen-dominant $\text{DOS}(E_F)$, and that some care must be taken in choosing the components. We show three such poor choices for the second model structure (all with $R=\text{Lu}$) in Fig. S1. The first example using $X=\text{Sr}$, $Y=\text{N}$, $Z=\text{H}$ (left) has a weakly dominant hydrogen DOS, and the minimum in the $\text{DOS}(E_F)$ implies a lower T_c . The DOS maxima are above E_F ; typically we find one can resolve this doping problem by pairing atoms corresponding to ionic insulators (i.e. II-VI, III-VI, rare earth nitrides, etc). In fact, insulating units for choices of X, Y tends to make the auxiliary cage inert. For example, the $X=\text{Ti}$, $Y=Z=\text{C}$ example (middle) features a Ti-d dominated $\text{DOS}(E_F)$ because the carbon does not gap the Ti; in fact TiC is not insulating. In the last example, we used a cubic semiconductor YbO to choose $X=\text{Yb}$, $Y=\text{O}$, $Z=\text{H}$. However, the unfilled f-shell in Yb participates at E_F . This can be understood as the YbO bandgap for thin films is only

0.25 eV [78], making it likely that the H/Lu environment hybridizes with the YbO units to eliminate the bandgap. Generally it appears wise to avoid compounds with unfilled f-shells. These counterexamples help inform us that only charge transfer or hole-doping alone does not yield the desired electronic structure.

3. Model Structure $(\text{RH}_{11})_2\text{X}_6\text{YZ}$ Inversion

We compute the effect of 'inverting' the structural motif of an RH_{11} unit protected by an X_6YZ cage shown in Fig. 5 by swapping the roles of the R and X atoms, visualized in Fig. S16. The PDOS of $(\text{CaH}_{11})_2(\text{Y}_6\text{OH})$ looks like an electron-doped version of $(\text{YH}_{11})_2(\text{Ca}_6\text{OH})$ despite the fact that the oxygen atoms are now near Y instead of Ca . Charge transfer from yttrium to oxygen now occurs, and while YO is not known to be insulating, several $(\text{Y},\text{H},\text{O})$ compounds are insulating. However, we note the ELF hydrogen networking isovalue ϕ_{iso}^{net} decreases from 0.53 to 0.49 upon this swap, which lowers the estimated T_c by ≈ 50 K to a range of 150 – 225 K.

4. Stability

We believe the best choices stability-wise for the cubic structure involve using well-known cubic semiconducting/insulating combinations where X also forms cubic alloys with R , such as $\text{RXY} = \text{YCaO/ScAlN}$. As an illustrative counterexample, if we choose $R=\text{Lu}$ and $X=\text{Na}$, the two are not known to form a cubic alloy, even though the Lu, Na radii are similar. We indeed find $\text{RXYZ} = \text{LuNaH}_2$ [equivalent to Fig. 4(b)] using the above structure is not even metastable. However, we have found doping some examples such as $(\text{ScH}_{11})_2(\text{Mg}_4\text{Li}_2\text{NH})$ results in hydrogen-dominant states at E_F with only a moderate tetragonal distortion away from cubic.

We note that quaternary hydride structures based on dense sphere packings were studied in Ref. [17], which have FCC-like packings of the large metal atoms but the locations of the hydrogen atoms differ from the structure presented in this work. Their $\text{ScY}_2\text{CaH}_{12}$ example had a hydrogen-dominant DOS and was found to be dynamically stable at ambient conditions with a computed T_c of 5.7 K. This low T_c despite the large hydrogen DOS is attributed to the large lattice constant and small electron-phonon coupling. Its enthalpy was found to be 78.6 meV/atom higher than that of the decomposition into ScH_3 , 2YH_3 , CaH_2 , and 0.5H_2 . Considering the computed T_c of FCC LuH_3 is much higher at ≈ 30 K despite a much lower DOS [25, 33, 45], we can infer the electron-phonon coupling associated with the hydrogen configuration in FCC RH_3 ($R=\text{Sc},\text{Y},\text{La},\text{Lu}$) is large, which in large part motivates the usage of FCC RH_3 as a parent structure.

a. Caveat - Hydrogen Stability It is possible that DFT-level relaxations may lead to the hydrogen forming

H_2 molecules, especially if the stabilizing X elements do not generally form XH_3 . We find this instability to occur for the $LuNa_3H_{12}$ case considered in Fig. 4(b) even when starting from the high-symmetry initial structure. If we perturb the initial structure away from its high-symmetry starting point, many $(RH_{11})_2(X_6YZ)$ examples also appear to suffer this instability. However, quantum and thermal effects can metastabilize such structures. Computational tools such as the SSCHA[55] have confirmed this to occur for $(LuH_{11})_2(Lu_6NH)$ [79] which we confirm suffers the same DFT-level instability towards H_2 molecule formation when perturbed away from the high-symmetry structure. We note such instabilities are likely occurring in $La[H,D]_{3-\delta}$ (which have multiple specific heat jumps in between 230-270 K) [80–83].

However, there is the matter of thermodynamic stability - if these compositions can support the amount of hydrogen suggested in the model structures at ambient conditions rather than some hydrogen decomposing into H_2 gas. For example, Mg_xSc_{1-x} alloys are known to hydrogenate as $Mg_xSc_{1-x}H_{3-x}$ [72]. This pattern holds true for $R=La$ as well[84]. While charged defects (which the X,Y,Z atoms can play the role of) can support adsorbed hydrogen[85, 86], it is unclear if this would meaningfully increase the hydrogen storage capacity in bulk $(RH_{11})_2(X_6YZ)$. Zero-point effects can be quite important for such calculations [87]. We note $Fm\bar{3}m$ MgH_3 requires 100 GPa to stabilize [88].

The thermodynamic stability of such compositions with respect to hydrogen content would be ensured if both R and X are known to support $[R/X]H_3$ phases at ambient pressures/temperatures.

a. Harmonic Phonons of Two Examples

In this section we discuss the two examples in Fig. S11 with the highest predicted T_c , $([La/Sc]H_{11})_2(Mg_6OH)$. The most relevant question for applications concerns whether or not these structures are dynamically stable at ambient pressures. While DFT does not account for temperature or quantum nuclear effects (which are large for hydrogen), it is still the most computationally feasible method for studying the vibrational properties of such a large cell. We use the `phonopy`[70] package to compute the harmonic phonons at Γ using the finite displacement method and plot the resulting phonon density of states.

In both cases studied in Fig. S2 there are predominantly hydrogen based modes that indicate instabilities (frequencies below zero). It is difficult to evaluate whether these hydrogen modes are truly unstable or not, due to their large quantum zero point motion and anharmonic corrections. In particular, systems with large electron-phonon coupling typically are unstable both to structural distortions and superconductivity. Extremely large electron-phonon coupling usually prefers the structural distortions [89], although the structural instabilities can be suppressed by disorder [31] and quantum nuclear

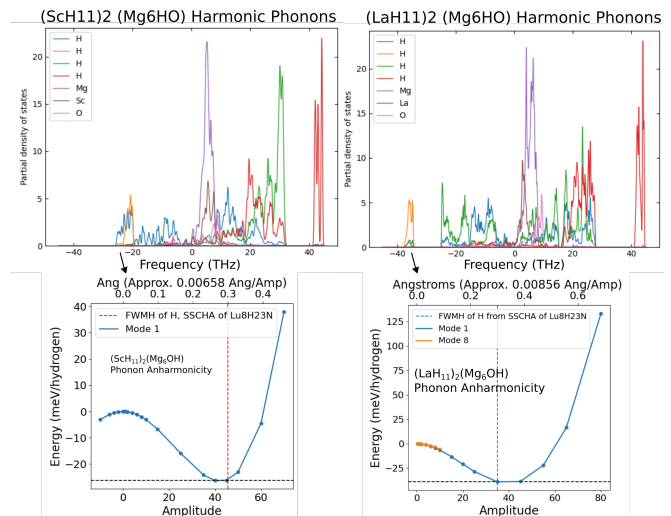


FIG. S2: Top: Atom-resolved phonon density of states (pDOS) in ambient conditions for $(RH_{11})_2(Mg_6OH)$ for $R=Sc/La$. There are four unique hydrogen atoms which we do not distinguish further for simplicity’s sake, but both octahedral and tetrahedral hydrogen participate in the unstable modes below 0 frequency. The simple acoustic sum rule (ASR) was used. Bottom: Collective-mode reaction-coordinate DFT analysis of the $([La/Sc]H_{11})_2(Mg_6OH)$ phonon mode with largest imaginary phonon frequency. The amplitude of modulation is also translated to approximate Angstroms moved per H atom by averaging H displacements. The full-width half-maximum (FWHM) is plotted from previous work on $Lu_8H_{23}N$ (A) [To be submitted] indicating the amount of quantum zero point motion of a typical hydrogen.

effects [45, 46].

We find the PBEsol functional for the phonon calculations does not change the results.

b. Anharmonicity Analysis

Despite the instabilities predicted by the harmonic phonon analysis above, it is possible that quantum zero point motion of the hydrogen atoms can stabilize the high-symmetry structure. This has been verified for some hydrides using the SSCHA method [46, 90]. In order to investigate this possibility, we perform a collective-mode reaction-coordinate analysis of the most unstable modes (largest imaginary part) of $([La/Sc]H_{11})_2(Mg_6OH)$. In a related work on $Fm\bar{3}m$ $Lu_8H_{23}N$ [91], this same analysis showed the instability to be very weak, which we argued would be easily stabilized by quantum zero point motion effects.

The results for $([La/Sc]H_{11})_2(Mg_6OH)$ are shown in Fig. S2, where the FWHM is displayed for hydrogen displacements from SSCHA data on $Fm\bar{3}m$ $Lu_8H_{23}N$, indicating the size of quantum zero point motion for a typical hydrogen atom in that system. The energy saved

along the reaction coordinates is much larger than that in $\text{Lu}_8\text{H}_{23}\text{N}$, and amplitude of the energy minimum is also much larger. The biggest differences in the La/Sc cases are that more of the hydrogen atoms contribute to $\text{DOS}(E_F)$ and that some octahedral hydrogen states end up with < 1 electron on average, likely due to the hole-doping effect of $X=\text{Mg}$. It is possible that electron-doping these examples would weaken these anharmonicities.

If we begin a relaxation from the minima outlined in Fig. S2, the hydrogen appear to disassociate from their positions and form H_2 molecules. Since LaMg_3 is experimentally known to typically only hydrogenate up to LaMg_3H_9 [84], it is possible a configuration with a higher R:Mg ratio is needed to sustain the high hydrogen density. In other words, we may want explore options with $X = \text{La}/\text{Sc}$ and merely doping $X'=\text{Mg}$.

5. Doping

While the parent structures/composition discussed in the main text are fairly flexible, our list of examples in Fig. S11 motivates a desire to account for doping due to the preponderance of large DOS peaks close to E_F . Electron/hole doping would be useful to tune E_F closer to a peak to maximize T_c , and isovalent doping with atoms of different sizes (i.e. $\text{La} \rightarrow \text{Sc}$) can help tune stability of the metal lattice and lattice constant, which can indirectly affect the electronic structure. For example, we note that the primary difference between $(\text{LaH}_{11})_2(\text{Mg}_6\text{OH})$ and $([\text{Y}/\text{Sc}]\text{H}_{11})_2(\text{Mg}_6\text{OH})$ is the lattice constant. The shrinking of the lattice constant of $(\text{LaH}_{11})_2(\text{Mg}_6\text{OH})$ leads to isolated hydrogen states more easily forming a metallic network, whose hybridization increases the hydrogen bandwidth, leading to the lower hydrogen $\text{DOS}(E_F)$ in the R=Sc,Y cases.

We therefore generalize the formula to include doping of the various parts of the formula:

$$\text{Doped Formula} = (R_{1-x}R'_xH_{11})_2(X_{6-n}X'_nY_{1-\gamma}Y'_\gamma Z_{1-\delta}Z'_\delta)$$

. The elements with a tick mark indicate the dopants, which are to be put in the same location as the parent atom.

Let us present an example of using such a formula. Going back to our $(\text{YH}_{11})_2(\text{Mg}_6\text{OH})$ example. If we wish to tune the lattice constant and hydrogen distances, we can go about this in various ways:

- Replace some O with S ($Y' = \text{S}$), increasing the lattice constant of the Mg_6O units on average.
- Replace some Mg with Ca ($X'=\text{Ca}$), increasing the overall lattice constant of the entire system more uniformly on average and increasing the thermodynamic stability of hydrogen in the system.
- Replace some Y with La ($R'=\text{La}$), increasing the size of the RH_{11} units on average.

On the other hand, if we wanted to electron-dope $(\text{YH}_{11})_2(\text{Mg}_6\text{OH})$ to tune E_F to approach the DOS peak 0.2 eV above E_F , we could accomplish this in multiple ways, with various pros and cons:

- Replace some O with H ($Y'=\text{H}$). The cons are that oxygen presence is vital to the tetrahedral hydrogen states at E_F , and that this may decrease the thermodynamic stability of the system since MgH_3 is thermodynamically unstable.
- Replace some Mg with Y/Sc ($Y'=\text{Y}/\text{Sc}$), leading to more electrons in the system. The cons are that this may lead to a distortion of the cubic cell, which may interfere with the metallic hydrogen sublattice chemistry.
- Replace some Y with Zr/Ce, which both may help electron-dope the system but risks weakening the superconductivity associated with the RH_{11} units.
- Replace some N/P with O/S in any systems using N/P.

If we wanted to hole-dope any of the above systems, we could go about it multiple ways:

- Replace some octahedral H with O/N/S/P ($Z' = \text{O}/\text{N}/\text{S}/\text{P}$). This risks forming O/N/S/P metal states which would interfere with the quantum interference phenomena raising $\text{DOS}_H(E_F)$.
- Replace some R with a normally 2+ oxidation state element (e.g. $R' = \text{Mg}/\text{Ca}/\text{Sr}$). This risks reducing the number of superconducting RH_{11} units.
- Replace some O/S with N/P in any systems using O/S.

Many of the electron/hole-doping examples listed above have cons, but should accomplish the desired doping without severely changing the electronic and stability properties if done in small quantities. An example of this is shown in Fig. S14 where we show how the electronic structure of $(\text{YH}_{11})_2(\text{Ca}_6\text{OH})$ remains unchanged aside from tuning E_F when electron doping with a pure electron (a), an additional Yttrium atom (b), or hole doping by replacing one of the 4b hydrogen with O. A larger amount of electron doping is necessary to tune E_F to the flat band in $(\text{LaH}_{11})_2(\text{Sr}_6\text{SH})$ at 0.7 eV above E_F , requiring four extra electrons. This result suggests that one should try simulating $(\text{LaH}_{11})_2(\text{Sr}_2\text{La}_4\text{SH})$ (choosing $X'=\text{La}, n=4$). As one can see, there are many tuning parameters in optimizing the electronic and structural properties for the best superconducting T_c and ideal stability properties. We leave more analyses of doping effects for future work.

Appendix SI-B: Methods

We performed DFT calculations primarily with the Quantum Espresso software package [40]. The SSSP

database [92] was used to vet pseudopotentials for convergence of the computed pressure, phonon frequencies, and formation energies. Accordingly, we chose rare earth pseudopotentials from Ref. [52], and the `pslibrary` pseudopotentials for most other elements [93]. We relaxed systems from the starting points in Fig. 1 using DFT-PBE which generally maintained high symmetry due to the symmetric starting point. Each relaxed structure had remaining forces under $1e-5$ Ry/Bohr, and energy differences were under $1e-5$ Ry. We did not relax structures again for the DFT+U calculations, as DFT+U typically worsens lattice parameter agreement when it corrects for electronic structure [94].

We used wavefunction plane-wave cutoffs of 90-100 Ry for the structures and charge density cutoffs of 360-400 Ry. We generally used tight k-meshes corresponding to 0.13 \AA^{-1} , but did convergence tests with more k-points as needed. We also used the optimized tetrahedron method [95] to evaluate the DOS. The `VESTA` code [96] was used for the visualizations of the ELF and ILDOS. ILDOS calculations performed integrations within a range of 5meV around E_F . We used `Quantum Espresso`'s default atomic projections for the PDOS calculations. We also performed comparisons of the PBE functional with the vdW-DF3-opt2 functional [97] for some of the calculations and saw no meaningful changes.

We performed DFT+U calculations with the U-values recommended in Ref. [93], which vetted the pseudopotentials and U-values with calculations on rare earth nitrides using the same codes and functional we use. We confirmed independently U-values for YN and ScN to match indirect band gaps. The ideal U-value is not tied to the atom, and in principle it should be structure-dependent. Nevertheless, we use a fixed U-value as it is generally difficult to find the ideal U-value for each structure, but U-dependence of the results are investigated. Ref. [52] also recommends $U=5.5$ eV for Lu_f electrons but use of this value did not significantly change the electronic properties near E_F .

Because we are using the networking-value T_c estimator[43], we perform DFT calculations using `Quantum Espresso` [40] at the PBE level[98] to match the calculations used to create the networking-value T_c estimator, as using other functionals would invalidate the usage of the estimator. We use the ϕ_{iso}^{net} computed for $n_{spin}=1$, $U=0$ as those are the parameters used to establish the estimator [43]

Appendix SI-C: Interface Superconductivity

Here we discuss further how the heterostructure designs we have implemented tie in to interface superconductivity. We focus on the $\text{Lu}_8\text{H}_{23}\text{N}$ stoichiometry but emphasize much of the below discussion generalizes to the model structures/stoichiometries considered in the main text.

In the context of $\text{Lu}_8\text{H}_{23}\text{N}$ (A) [37], nitrogen doping

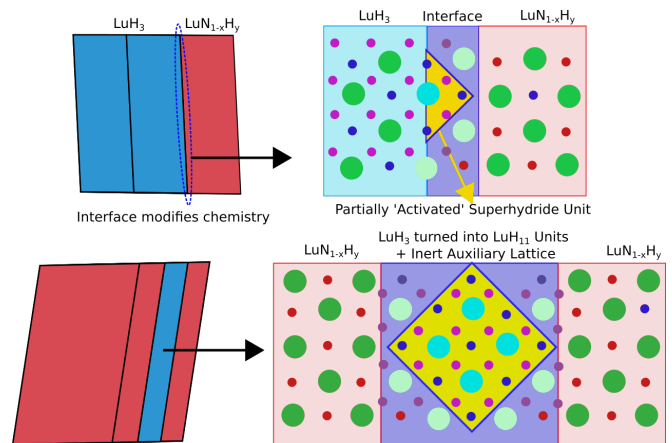


FIG. S3: Top: A model of the interface between Fm3m LuH_3 and $\text{LuN}_{1-x}\text{H}_y$ (top) illustrating how the altered charge dynamics at the interface results in certain hydrogen/lutetium atoms being closer to neutral charge (H atoms around 1.05-1.1 electrons) which begins to 'prep' a superhydride phase. Bottom: A bi-interface which applies these charge inhomogeneities on either side of FCC LuH_3 , leading to the formation of units of LuH_3 which chemically act more like LuH_{10+x} .

produces LuNH_2 units where the nitrogen preferentially ionically bonds with Lu, with hydrogen losing charge and weakening the LuH bonds. This causes the hydrogen to instead hybridize with each other to form a metallic hydrogen sublattice, generally surrounding the Lu atoms, forming H_{11-n} 'cages' around Lu. This ensures all the hydrogen atoms in the LuH_{11} units are contributing to the hydrogen metallic network.

This implies that interfaces between regions with nitrogen doping and those without will have metallic hydrogen sublattices. In $\text{LaAlO}_3/\text{SrTiO}_3$ and related heterostructures, superconductivity similarly is induced on the interface due to polarization effects [99–101]. In the case of $\text{FeSe}/\text{SrTiO}_3$, T_c is enhanced dramatically[102].

We visualize such heterostructure form for $\text{Lu}_8\text{H}_{23}\text{N}$ (A) in Fig. S3. Due to the strong LuN bonding, tetrahedral hydrogen instead bond with surrounding hydrogens. This allows the hydrogens on the interface to form metallic bonds with LuH_3 within the LuH_3 layer, leading to units of LuH_3 which instead chemically are similar to the superhydride state. As shown in the bottom of Fig. S3, this effect is enhanced when the LuH_3 layer is surrounded on two sides. However, we believe this effect is strongest in small units of LuH_3 surrounded by the $\text{LuN}_{1-x}\text{H}_y$ layers (with optimal choice of x,y), as is the case in $\text{Lu}_8\text{H}_{23}\text{N}$ (A), which is partially why $\text{Lu}_8\text{H}_{23}\text{N}$ (A) is capable of generating a $\text{DOS}(E_F)$ which is comparable to that of LuH_{11} .

We note that the transition widths observed in the experiments on Lu-H-N [35, 36] are very small, similar to Josephson junctions of cuprates [103]. It is possible that regions of Lu-H-N which are under/overdoped (with

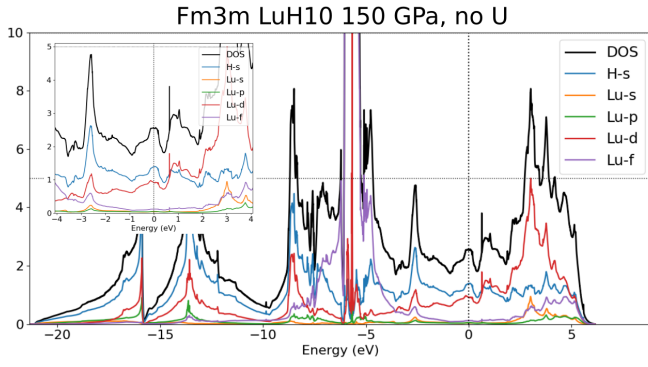


FIG. S4: Computed PDOS of Fm3m LuH₁₀ at 150 GPa.

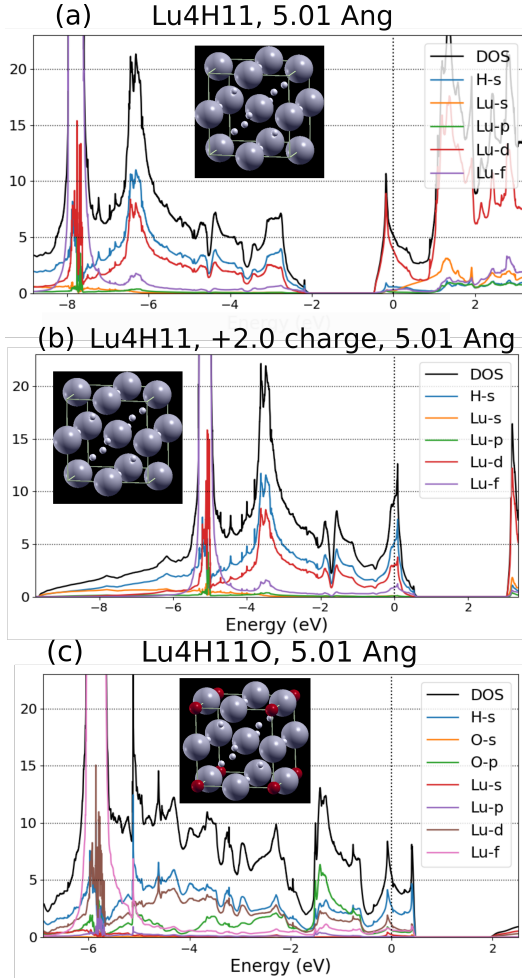


FIG. S5: PDOS with $U=7.5$ eV of Pm3m Lu₄H₁₁ (a), Lu₄H₁₁-2+ (b), and Lu₄H₁₁O (c).

varying H,N densities) may still serve as bridges between superconducting regions, as we note in the cuprates there is a giant proximity effect of SNS junctions [104, 105] (with N a underdoped cuprate whose thickness exceeding the coherence length).

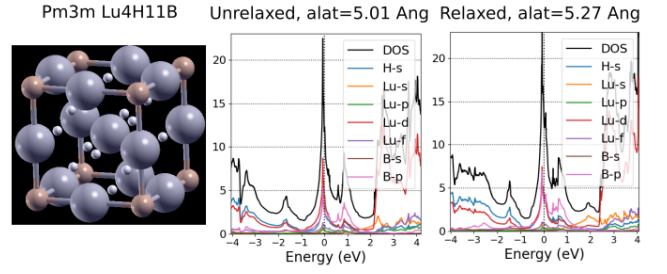


FIG. S6: PDOS of Lu₄H₁₁B with DFT+U, $U=7.5$ eV. There is a flat band at E_F of hybridized character which persists upon relaxation of the unit cell.

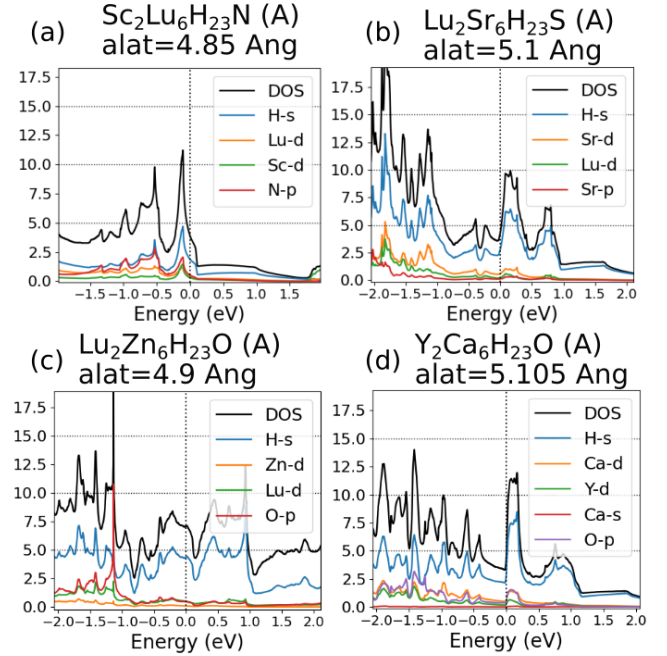


FIG. S7: The PDOS calculated for (a) (ScH₁₁)₂(Lu₆NH) with alat 4.85Å, (b) (LuH₁₁)₂(Sr₆HS) with alat 5.1Å, (c) (LuH₁₁)₂(Zn₆HO) with alat 4.9Å, and (d) (YH₁₁)₂(Ca₆OH) with alat 5.18Å

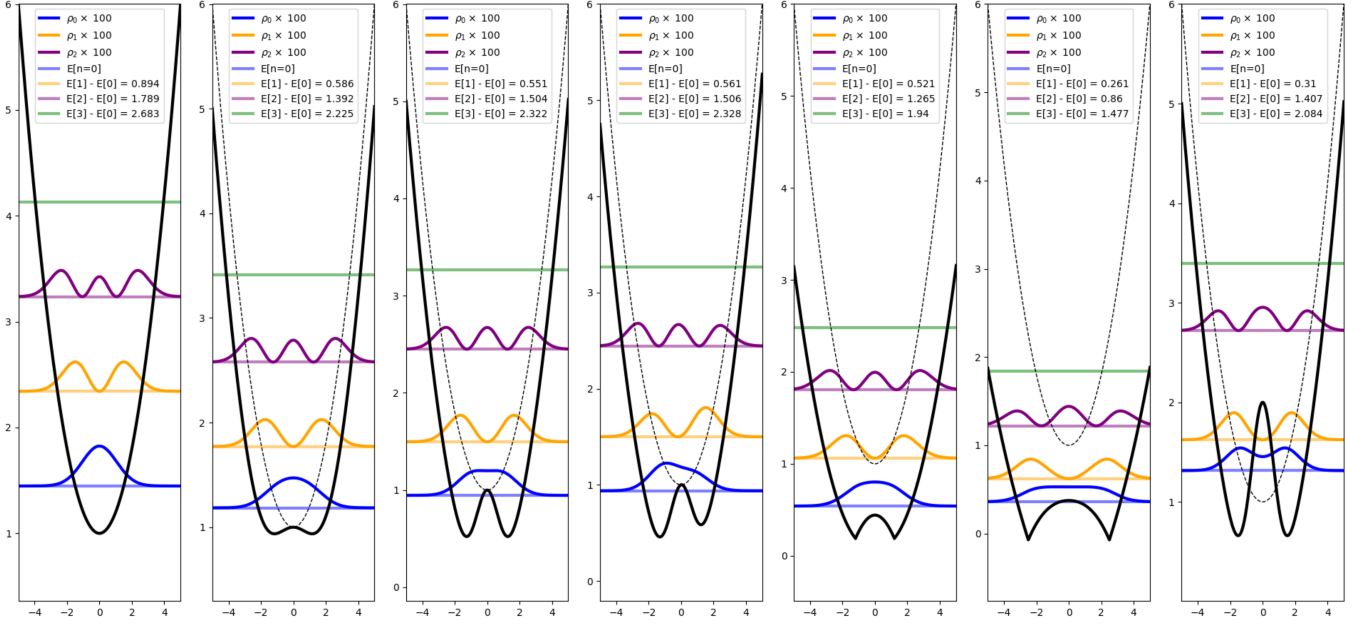
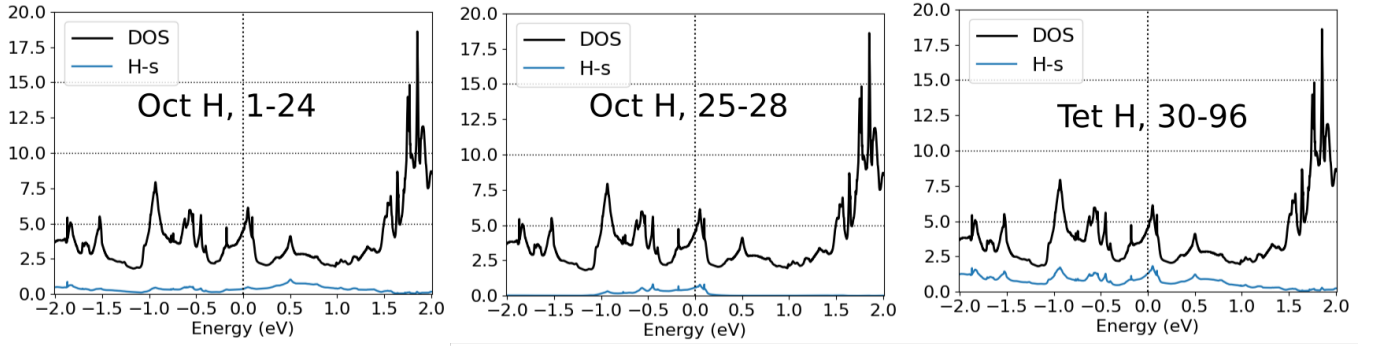


FIG. S8: Computed ground state (ground) and excited state densities (yellow, purple) for a variety of anharmonic potentials in the 1D Schrodinger equations.

20 GPa PDOS, undistorted structure



20 GPa PDOS, distorted structure

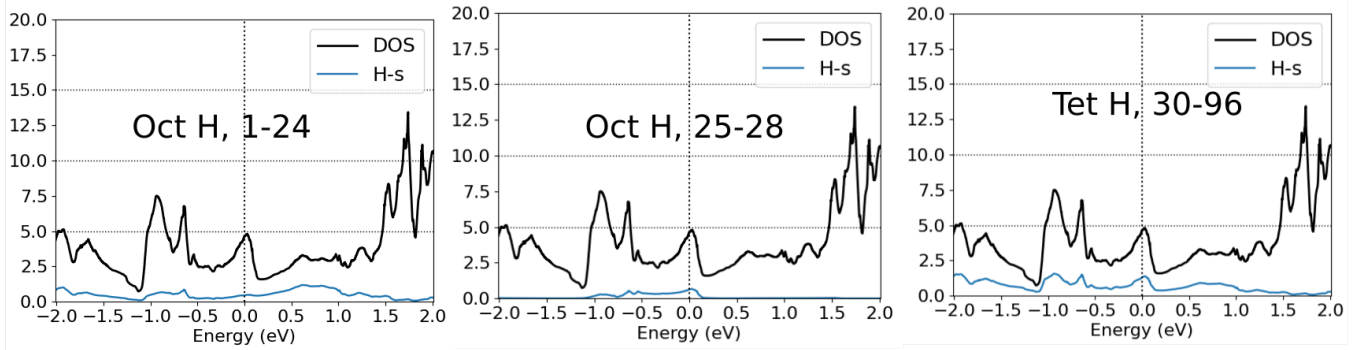


FIG. S9: PDOS of $(\text{CaH}_{11})\text{Sc}_6\text{NH}$ resolved into the unique types of hydrogen in the system. The 24d-hydrogen, 4b hydrogen, and tetrahedral hydrogen all contribute nontrivially to $\text{DOS}(E_F)$, before and after the structural distortion (see main text).

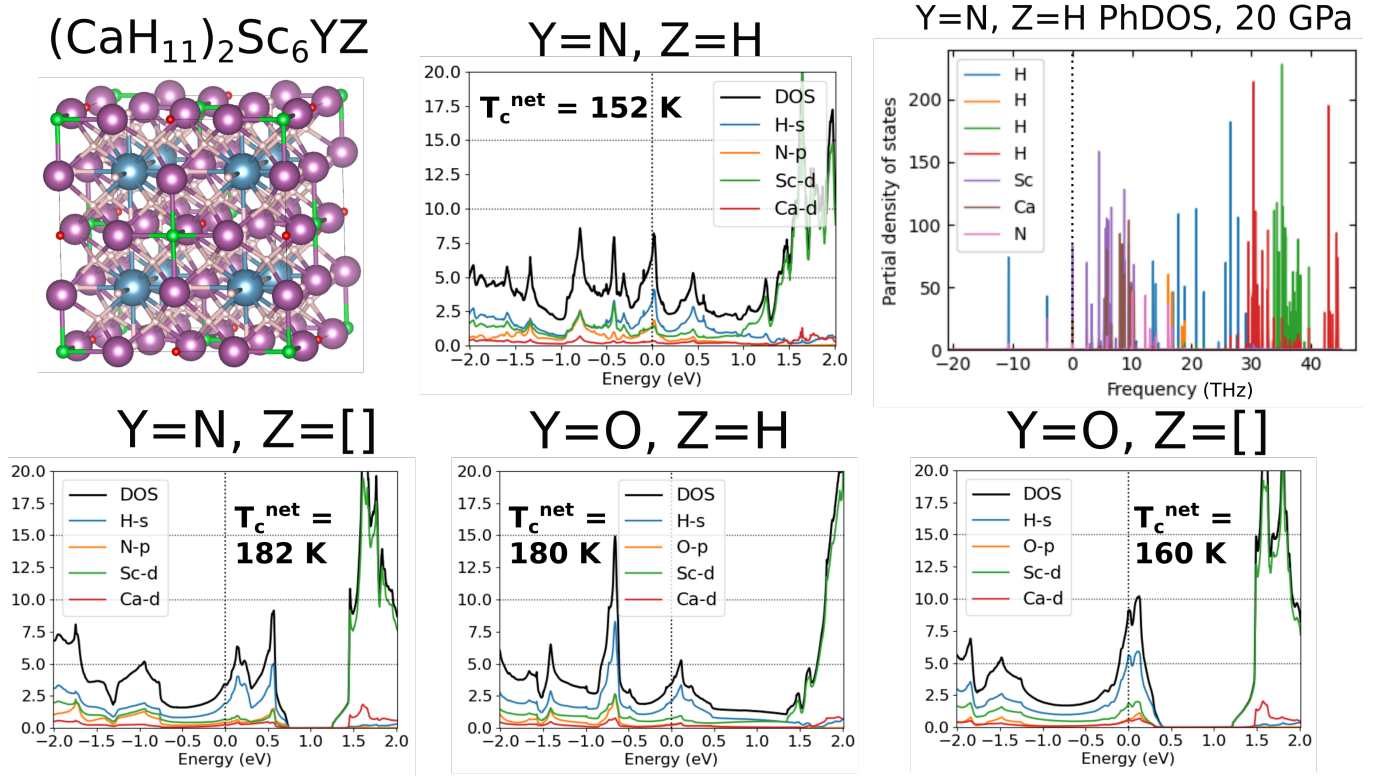


FIG. S10: PDOS of $(\text{CaH}_{11})_2\text{Sc}_6\text{YZ}$ for various Y,Z, and their associated T_c^{net}

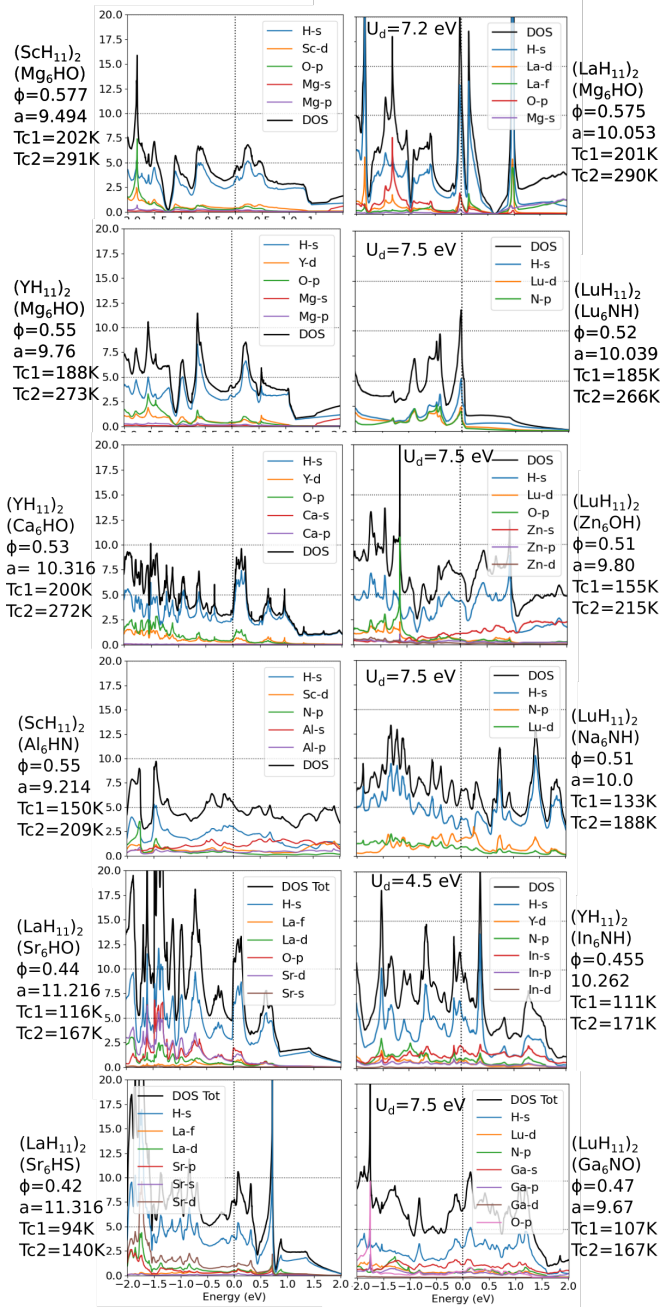


FIG. S11: The PDOS calculated for twelve quaternary hydride compositions using the formula discussed in the text. For each, the lattice constant, computed ϕ_{iso}^{net} , and estimated T_c s are listed. Both columns are ordered from highest estimated T_c (top) to lowest (bottom). For structures in the left column +U was not applied, and the structures in the right column had the indicated U-value applied for the R atoms. All structures were relaxed using PBE from the high-symmetry starting point defined by the structure formula.

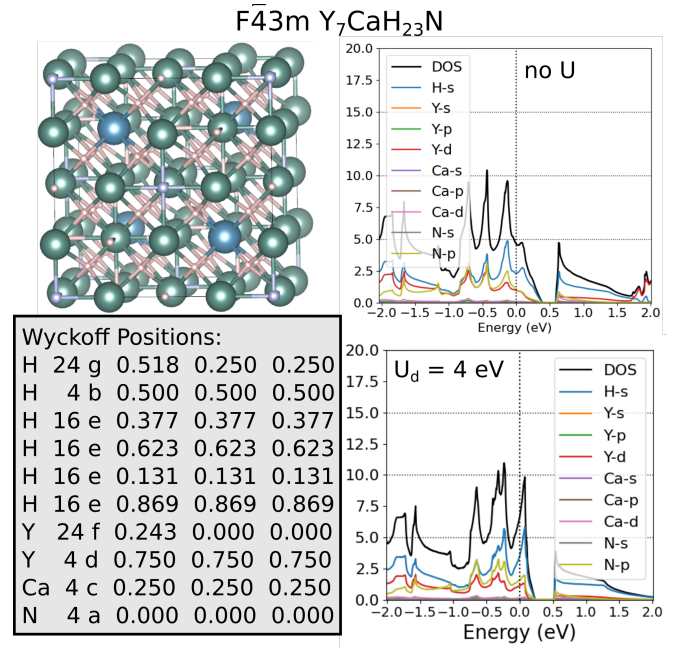


FIG. S12: Structure and PDOS of (YCaH₂₂)(Y₆NH) without and with $U = 4$ eV, and lattice constant 10.244 Å. The ϕ_{iso}^{net} increases to 0.56 due to the 24g-H compressing toward the 4d-Y upon Ca doping. The networking-value T_c^{net} we obtain using the Quantum Espresso projections is 180 K.

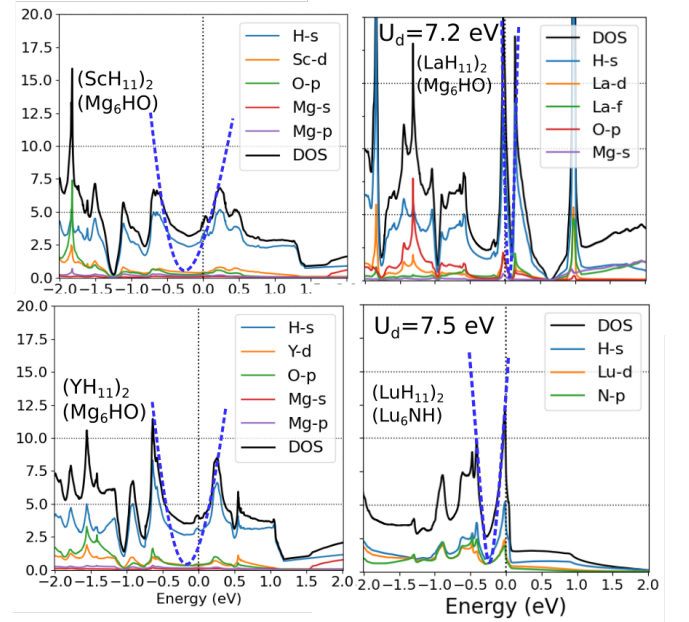


FIG. S13: PDOS of four examples following the second model structure (RH₁₁)₂X₆YZ with the common U-shaped DOS near E_F highlighted.

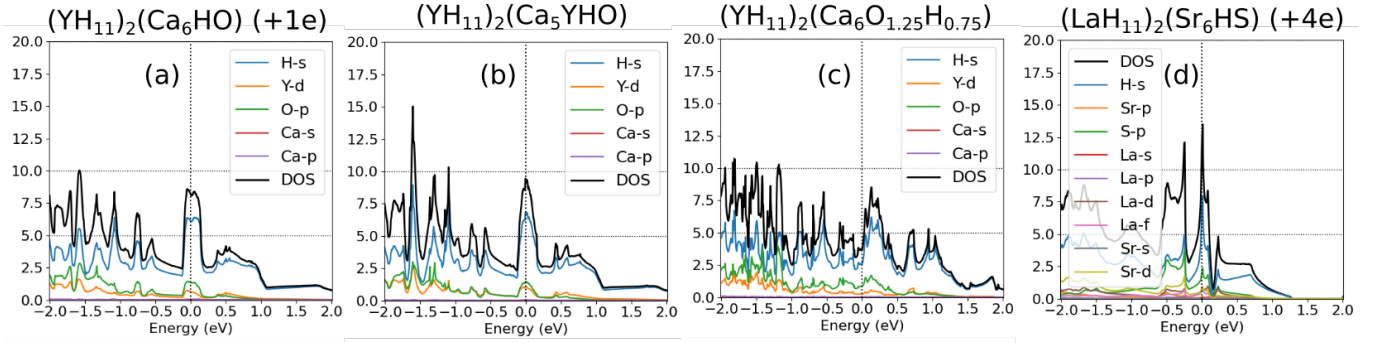


FIG. S14: PDOS calculated for doped variants of two example compositions shown in Fig. S11. Relaxation with dopants was not performed. (a) $(\text{YH}_{11})_2(\text{Ca}_6\text{OH})$ with an extra electron added to the 32-atom primitive cell with compensating uniform background charge. (b) $(\text{YH}_{11})_2(\text{Ca}_5\text{YOH})$ (choosing $X'=Y$). (c) $(\text{YH}_{11})_2(\text{Ca}_6\text{O}_{1.25}\text{H}_{0.75})$ (choosing $Z'=O$). (d) $(\text{LaH}_{11})_2(\text{Sr}_6\text{SH})$ with four extra electrons added to the 32-atom primitive cell.

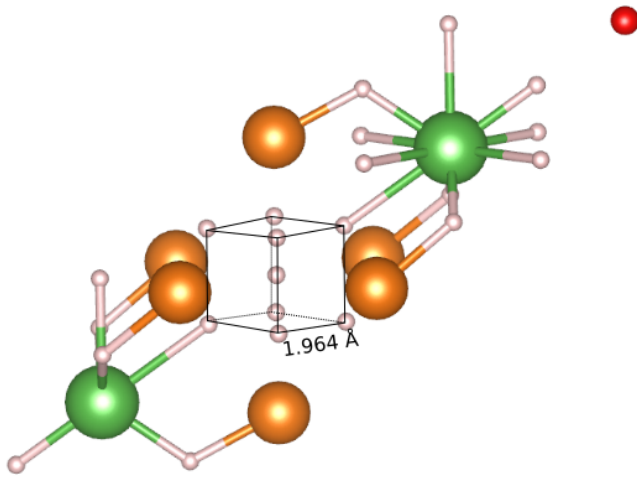


FIG. S15: Primitive cell of $(\text{LaH}_{11})_2(\text{Mg}_6\text{OH})$ with an inner hydrogen cage visualized.

R_6YZ Charge-Donating Pocket

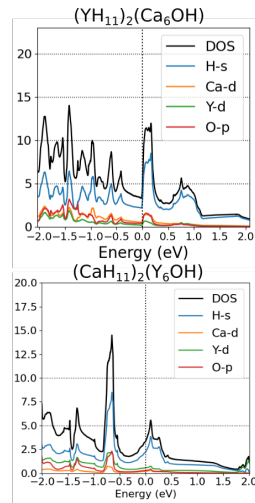
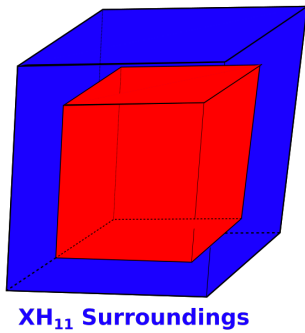


FIG. S16: We picture inverting the role of the R and X atoms (left) since the interface chemistry should be similar. Indeed, our example (right) shows that $(\text{YH}_{11})_2(\text{Ca}_6\text{OH})$ (lattice constant 5.158 Å) and the swapped X,R role version $(\text{CaH}_{11})_2(\text{Y}_6\text{OH})$ (lattice constant 5.119 Å) have a very similar DOS near E_F , with the extra electrons simply providing a hole-doping effect.

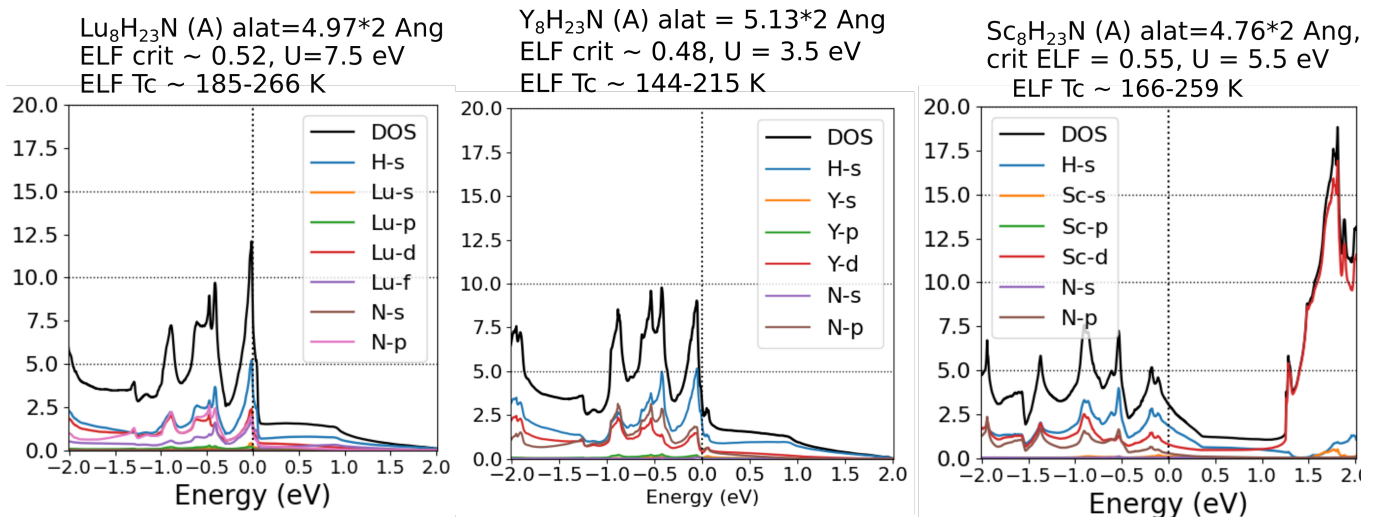


FIG. S17: PDOS of $(\text{RH}_{11})_2(\text{R}_6\text{NH})$ using the parent structure